ATOMIC LAYER DEPOSITION OF METAL OXIDE THIN FILMS AND NANOSTRUCTURES

A THESIS
SUBMITTED TO MATERIALS SCIENCE AND NANOTECHNOLOGY PROGRAM
OF THE GRADUATE SCHOOL OF ENGINEERING AND SCIENCE
OF BILKENT UNIVERSITY
IN PARTIAL FULFILLMENT OF THE REQUIREMENTS
FOR THE DEGREE OF
MASTER OF SCIENCE

By
İnci Dönmez
January, 2013

I certify that I have read this thesis and that in my opinion it is fully adequate, in scope and in quality, as a thesis for the degree of Master of Science.

_____

Assist. Prof. Dr. Necmi Bıyıklı (Supervisor)

I certify that I have read this thesis and that in my opinion it is fully adequate, in scope and in quality, as a thesis for the degree of Master of Science.

_____

Assist. Prof. Dr. Tamer Uyar

I certify that I have read this thesis and that in my opinion it is fully adequate, in scope and in quality, as a thesis for the degree of Master of Science.

_____

Assoc. Prof. Dr. H. Emrah Ünalan

Approved for the Graduate School of Engineering and Science:

_____

Prof. Dr. Levent Onural

Director of Graduate School

ABSTRACT

ATOMIC LAYER DEPOSITION OF METAL OXIDE THIN FILMS AND NANOSTRUCTURES

İnci Dönmez

M.S. in Materials Science and Nanotechnology

Supervisor: Assist. Prof. Dr. Necmi Bıyıklı

January, 2013

With the continuing scaling down of microelectronic integrated circuits and increasing need for three-dimensional stacking of functional layers, novel or improved growth techniques are required to deposit thin films with high conformality and atomic level thickness control. As being different from other thin film deposition techniques, atomic layer deposition (ALD) is based on self-limiting surface reactions. The self-limiting film growth mechanism of ALD ensures excellent conformality and large area uniformity of deposited films. Additionally, film thickness can be accurately controlled by the number of sequential surface reactions.

Gallium oxide (Ga_2O_3) thin films were deposited by plasma-enhanced ALD (PEALD) using trimethylgallium as the gallium precursor and oxygen plasma as the oxidant. A wide ALD temperature window was observed from 100 to 400 °C, where the deposition rate was constant at ~0.53 Å/cycle. The deposition parameters, composition, crystallinity, surface morphology, optical and electrical properties were studied for as-deposited and annealed Ga_2O_3 films. In order to investigate the electrical properties of the deposited films, metal-oxide-semiconductor capacitor structures were fabricated for a variety of film thicknesses and annealing temperatures. Ga_2O_3 films exhibited decent dielectric properties after crystallization upon annealing. Dielectric constant was increased with film thickness and decreased slightly with increasing annealing

temperature. As an additional PEALD experiment, deposition parameters of In_2O_3 thin films were studied as well, using the precursors of cyclopentadienyl indium and O_2 plasma. Initial results of this experiment effort are also presented.

Accurate thickness control, along with high uniformity and conformality offered by ALD makes this technique quite promising for the deposition of conformal coatings on nanostructures. This thesis also deals with the synthesis of metal oxide nanotubes using organic nanofiber templates. Combination of electrospinning and ALD processes provided an opportunity to precisely control both diameter and wall thickness of the synthesized nanotubes. As a proof-of-concept, hafnia (HfO_2) nanotubes were synthesized using three-step approach: (i) preparation of the nylon 6,6 nanofiber template by electrospinning, (ii) conformal deposition of HfO_2 on the electrospun polymer template via ALD using the precursors of tetrakis(dimethylamido)hafnium and water at 200 °C, and (iii) removal of the organic template by calculation to obtain freestanding HfO_2 nanotubes (hollow nanofibers). When the same deposition procedure was applied on nanofibers with different average fiber diameters, thinner HfO_2 wall thicknesses were obtained for the templates having smaller diameters due to insufficient exposure of precursor molecules to saturate their extremely large surface area. Thus, "exposure mode" was applied to obtain the desired wall thickness while coating high-surface area nanofibers. We present the experimental efforts including film deposition parameters, structural, elemental, and morphological properties of HfO_2 nanotubes.

Keywords: Plasma-Enhanced Atomic Layer Deposition, Gallium Oxide, Indium Oxide, Hafnium Oxide, Thin Films, Nanotubes

ÖZET

METAL OKSİT İNCE FİLM VE NANOYAPILARIN ATOMİK KATMAN KAPLAMA YÖNTEMİ İLE BÜYÜTÜLMESİ

İnci Dönmez

Malzeme Bilimi ve Nanoteknoloji, Yüksek Lisans

Tez Yöneticisi: Yrd. Doç. Dr. Necmi Bıyıklı

Ocak, 2013

Mikroelektronik entegre devrelerin devam eden küçülmesiyle birlikte üç boyutlu fonksiyonel tabakalara olan ihtiyaç artmış, yüksek konformalite ve atomik seviyede kalınlık kontrolu sağlayan orjinal ve geliştirilmiş büyütme teknikleri gerekmiştir. Diğer ince film kaplama tekniklerinden farklı olarak, atomik katman kaplama ("Atomic Layer Deposition", ALD) yöntemi kendini sınırlayan reaksiyonlara dayanmaktadır. ALD'nin kendini sınırlayan büyütme mekanizması mükemmel konformalite ve geniş alanda düzgün kaplamalara imkan sağlamaktadır. Ayrıca, film kalınlığı tam olarak ardışık yüzey reaksiyonların sayısını değiştirerek kontrol edilebilmektedir.

Galyum oksit (Ga_2O_3) ince filmler $Ga(CH_3)_3$ ve oksijen (O_2) plazma öncü maddeleri kullanılarak plasma yardımcı atomik katman kaplama (PEALD) yöntemi ile büyütülmüştür. 0.53 Å/devir sabit kaplama hızı ile 100-400 °C aralığında geniş ALD sıcaklık penceresi gözlemlenmiştir. Büyütülen Ga_2O_3 filmlerin kaplama parametreleri, kompozisyon, kristalinite, yüzey morfolojisi, optik ve elektriksel özellikleri tavlanmadan önce ve sonra karakterize edilmiştir. Büyütülen filmlerin elektriksel özelliklerinin araştırılması amacıyla, farklı film kalınlığı ve tavlama sıcakları içeren metal-oksit-yarıiletken kapasitör yapıları imal edilmiştir. Ga_2O_3 filmler tavlama sonrasında etkili dielektirik özellikler sergilemiştir. Dielektrik sabiti film kalınlığı ile artmış ve artan tavlama sıcaklığı

ile hafif azalmıştır. Ek PEALD deneyi olarak, indiyum oksit (In_2O_3) ince filmlerin kaplama parametreleri C_5H_5In ve O_2 plasma öncüleri kullanılarak çalışılmıştır. Bu deneylere ilişkin ilk sonuçlar da bu tez kapsamında verilmiştir.

ALD, hatasız kalınlık kontrolü, yüksek homojenlik ve konformalite özellikleri sayesinde nanoyapıların üzerine konformal kaplamalar için oldukça umut verici bir kaplama yöntemi haline gelmiştir. Bu tez çalışması, aynı zamanda, organik nanolif yapıları kullanılarak metal oksit nanotüplerin sentezlenmesini de içermektedir. Elektroeğirme ve ALD yöntemleri bir arada kullanıldığında, sentezlenen nanotüplerin hem iç çaplarını, hem de duvar kalınlıklarını düzgün bir şekilde kontrol etme imkanı sağlanmıştır. Kavram ispatı olarak, HfO_2 nanotüplerlerin sentezi üç adımda gerçekleştirilmiştir: (i) elektroeğirme yöntemi ile nylon 6,6 nanoliflerin hazırlanması, (ii) ALD ile $Hf(NMe_2)_4$ ve su öncüleri kullanılarak nanoliflerin üzerine 200 °C de konformal HfO_2 katmanının kaplanması, (iii) nanoliflerin kalsinasyon yöntemi ile kaldırılması sonucunda içi boş serbest HfO_2 nanotüplerin elde edilmesi. Aynı prosedür farklı ortalama lif çaplarına uygulandığında, daha küçük çaplı fiberler için beklendiğinden daha az duvar kalınlığı elde edilmiştir. Bunun sebebi geniş alanlı yüzeylerde öncünün maruz kalma süresinin yetersiz kalması ile açıklanmıştır. Bu nedenle, geniş yüzey alanları nanoyapıların kaplanmasında istenilen duvar kalınlığını elde etmek için "exposure mode" adı verilen farklı bir kaplama yöntemi uygulanmıştır. HfO_2 nanotüpler elde etmek için gerekli film kaplama parametreleri ve elde edilen nanotüplerin yapısal, elementel ve yüzeysel karakterizasyonları sunulmştur.

Anahtar Sözcükler: Plasma-Yardımlı Atomik Katman Kaplama (PEALD), Galyum Oksit, İndiyum Oksit, Hafniyum Oksit, İnce Filmler, Nanotüpler

To my family and friends...

Acknowledgement

I wish to thank my advisor, Assist. Prof. Dr. Necmi Bıyıklı, for his valuable guidance, encouragement and criticism throughout the development of this work. I would like to thank especially my committee members, Assist. Prof. Dr. Tamer Uyar and Assoc. Prof. Dr. H. Emrah Ünalan for their thorough reading of this thesis and helpful comments. In addition, thanks to Assist. Prof. Dr. Aykutlu Dana for his worthy advices.

I would like to express my deep appreciation to Çağla Özgit-Akgün, who showed me the road and helped to get me on the path. She has oriented and supported me with promptness and care, and has always been encouraging in times of difficulties, and most importantly, has made me feel a friend. Without her guidance and persistent help, this thesis would not have been possible.

Special thanks to M. Alican Noyan for his endless support and great patience. Even in hard times, he was always there to encourage me.

I would also like to thank all my mates & colleagues who contributed to my research experience and made it a joy for me including Engin, Feyza, Deniz, Burcu, Levent, Adem, Enver, Fatih Bilge, Fatma, Ahmet, Gürkan, Alper, Temmuz, Mustafa, Ayşe, Elif, Enes, Sami, Furkan... I would particularly like to thank Fikret Piri, Semih Yaşar and Mustafa Güler, I have learned a lot from them. I am also indebted to Handan Acar and Mustafa Ürel for UV-VIS and AFM measurements, respectively.

Finally, warmest thanks go to my parents, grandparents and especially sisters Merve and Melike for their continuous love, support and belief in me.

Contents

List of Figures

List of Tables

Chapter 1

Introduction

1.1 Historical Background

Atomic layer deposition (ALD) is a special type of chemical vapor deposition (CVD) technique, where thin film deposition is based on sequential self-limiting surface reactions. Due to this reaction mechanism, thickness control at the atomic scale and excellent conformality can be achieved at low deposition temperatures.

First studies regarding to ALD principle were published in the early 1960s with the name of "Molecular Layering" by a Soviet research group from the supervision of Prof. V.B. Aleskovskii, who is a corresponding member of the Russian Academy of Sciences [1]. In 1970s, ALD was world widely introduced under the name atomic layer epitaxy (ALE) by Dr. Suntola and his co-workers, and its first successful application was for the deposition of zinc sulfide for thin film electroluminescent (TFEL) flat panel displays [2]. Manufacturing of TFEL displays started in 80's and first products were used at the Helsinki Airport starting from 1983. Along its history, the ALD technique is referred with many

different names to emphasize different properties of this unique technique. Common names used to refer ALD are listed in Table 1.1. The name of ALD, the most widely used one, dates back to early 1990s.

Table 1.1: Alternative names of ALD. [3]

Name	**Abbreviation**
Atomic layer chemical vapor deposition	ALCVD
Atomic layer deposition	ALD
Atomic layer epitaxy	ALE
Atomic layer evaporation	ALE
Atomic layer growth	ALG
Chemical assembly	
Digital layer epitaxy	DLE
Molecular deposition	
Molecular lamination	
Molecular layer epitaxy	MLE
Molecular layering	ML
Molecular stratification	

In 1991, the first study using plasma-enhanced atomic layer epitaxy was reported by De Keijser and Van Opdorp from Philips Research Laboratories in Eindhoven, the Netherlands [4]. In their study, hydrogen radicals were generated in a remote microwave-induced plasma and used for the deposition of gallium arsenide. Starting from mid-90s, ALD has attracted a significant interest due to the continuing scaling down of microelectronic devices. In 2007, Intel Corporation has realized its 45 nm CMOS technology by using ALD to deposit Hf-based high-k thin film as the gate dielectric layer [5].

1.2 Motivation

Semiconductor integrated circuit (IC) technology is continuously scaling down to smaller transistor gate sizes, and the ascending number of stacked layers increase the three-dimensional architectural complexity. Therefore, the need for high-quality and conformal ultra-thin films together with the development of suitable deposition techniques increased. Deposition of uniform thin films on large-area substrates has also become an important necessity for the IC industry. These specific requirements, which cannot be fulfilled using common physical vapor deposition (PVD) or CVD methods, can be met by ALD. The interest in this particular thin film deposition method, therefore, increased starting from the mid-90s.

Unlike other CVD methods, ALD is based on the saturative surface reactions, which results in a self-limiting growth mechanism. As a result, excellent conformality and large-area uniformity in addition to accurately controlled film thickness are inherently obtained. The processing temperatures can also be kept low, which makes ALD very applicable for a wide range of substrates including transparent and flexible polymers.

1.3 Objectives

This thesis mainly focuses on the optimization of plasma-enhanced ALD parameters for the deposition of gallium oxide (Ga_2O_3) thin films using trimethylgallium (TMG) and oxygen (O_2) plasma. This specific combination of precursors is reported for the first time in this thesis. While developing a recipe, the aim was to gain knowledge on the parameters controlling the resulting material properties. For this purpose, a detailed systematic materials characterization study was carried out on the deposited Ga_2O_3 thin films. In

addition, deposition of indium oxide (In_2O_3) using the precursors of cyclopentadienyl indium (CpIn) and O_2 plasma was aimed.

Another goal of this work was to demonstrate the effectiveness of the ALD method to create metal oxide nanostructures. To achieve this goal, hafnia (HfO_2) nanotubes were synthesized using a template-based method, which combines the electrospinning and ALD processes. HfO_2 nanotubes were synthesized and characterized in detail as a proof of concept study.

1.4 Thesis Overview

In this part, a brief outline of the thesis is given. Chapter 2 presents a review of ALD and literature overview for the deposition of Ga_2O_3 and In_2O_3 thin films and HfO_2 nanostructures. Chapter 3 explains the experimental procedure that was followed for the deposition of metal oxides together with the characterization equipments used. Chapter 4 discusses the growth of Ga_2O_3 thin films and characterization of these films in terms of their morphological, structural, elemental, optical and electrical properties. A brief optimization and characterization study for In_2O_3 thin films is also included. Details regarding to the template-based synthesis and characterization of HfO_2 nanotubes are summarized in this chapter as well. Finally, Chapter 5 concludes the thesis.

Chapter 2

Theoretical Background and Literature Overview

In this chapter, a brief historical perspective on ALD research will be introduced and the film-growth mechanisms of ALD will be discussed. Afterwards, ALD technique will be compared with alternative thin film deposition methods and performance metrics will be presented. In addition, ALD precursor selection criteria will be described, which will be followed by a brief literature overview on Ga_2O_3 thin film materials and their deposition using plasma-enhanced ALD technique. In the last section, synthesis of metal oxide nanotubes by combining electrospinning and ALD processes will be described and the characteristics of the resulting nanostructures will be summarized.

2.1 An Overview on Atomic Layer Deposition

ALD is a special type of chemical vapor deposition (CVD) technique, which is based on successive, self-limiting, surface-controlled reactions from the gas phase to produce conformal coatings either on flat substrates or three-dimensional nanostructured templates. In ALD, different from the other CVD techniques, each precursor pulse is separated by purging periods, resulting in surface saturation with a monolayer of that precursor. This unique film growth mechanism brings with it advantages such as high uniformity and conformality, and high-precise film thickness control at the atomic scale [6].

2.1.1 Mechanism

The principle of ALD method is based on alternating surface reactions, which result in saturated surfaces. A single ALD cycle deposits a monolayer of film material as a result of this self-limiting growth mechanism, and it consists of the following four steps:

1) A self-terminating reaction of the first reactant (precursor,"Reactant A" in Figure 2.1).
2) Evacuation or purging by inert gas flow to remove non-reacted precursors and byproducts from the chamber.
3) Exposure of the second reactant species (typically oxidant or reagents, "Reactant B" in Figure 2.1) which again results in a self-terminating reaction.
4) Evacuation or purging by inert gas flow to remove the excess reactants and byproduct molecules from the chamber.

In order to understand the detailed mechanism of this four-step unit growth cycle, extensive amount of knowledge in surface science, reaction kinetics and mass transport is required. One ALD reaction cycle is illustrated

schematically in Figure 2.1. Each precursor exposure step (1 and 3) saturates the surface with a monolayer of that precursor. In order to obtain ALD growth, self-limiting surface reactions must be the dominant processes unlike the deposition processes, where non-self-limiting gas-phase reactions takes place (CVD or PVD).

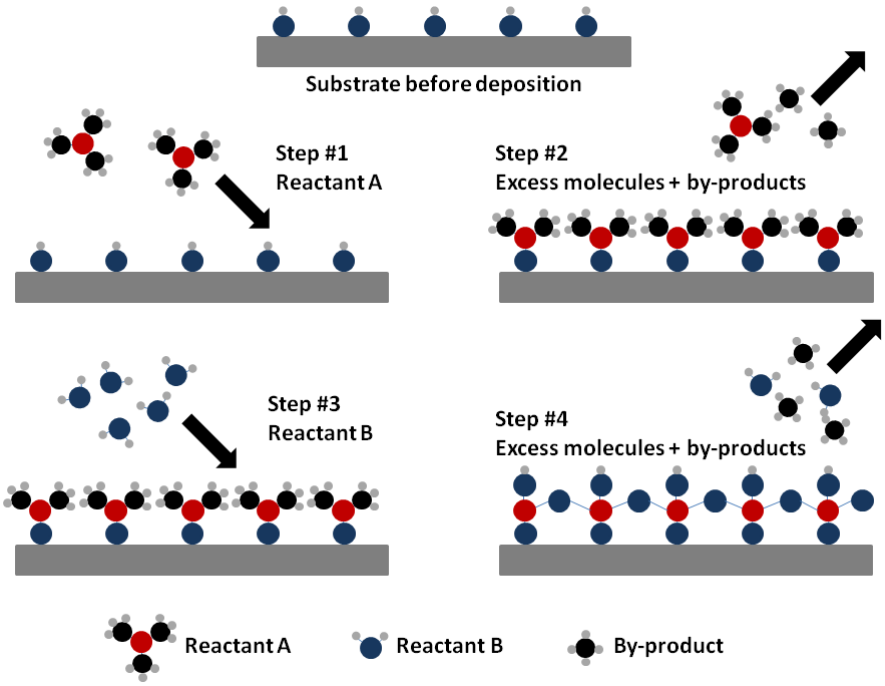

Figure 2.1: Schematic illustration of a single ALD cycle.

Following the completion of one cycle, surface is back to its original state and is ready for following cycles. This growth mechanism results in a layer-by-layer deposition at the atomic scale, and therefore gives accurate thickness control. Since the amount material deposited is constant for each ALD cycle, a film with desired thickness can be simply achieved by repeating the reaction cycles.

In ALD, three types of chemisorption mechanisms occur between the compound reactants via self-terminating reactions [7].

i) Ligand exchange

$$\mathrm{II} - a + \mathrm{ML_{z(g)}} \rightarrow \mathrm{II} - \mathrm{ML_{z-1}} + a\mathrm{L_{(g)}}$$

In *ligand exchange* mechanism (Figure 2.2), the reactant molecule (ML_z) is split and one of its ligands (L) combines with a surface group (II-a). As a result, a volatile compound (aL) is released as the reaction byproduct. Ligand exchange reaction can also take place between the surface group and adsorbed ML_{z-y} complex, but such a reaction does not result in bonding of more metal species on the surface.

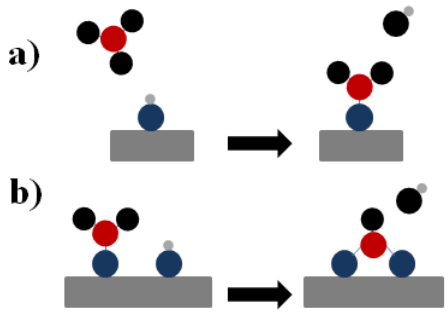

Figure 2.2: (a) Ligand exchange reaction of the ML_z reactant with surface "-*a*", releasing gaseous byproduct *a*L. (b) Ligand exchange can also occur between the surface group and adsorbed ML_{z-y} complex.

ii) Dissociation

$$\mathrm{IIM'} - \mathrm{ZII} + \mathrm{ML_{z(g)}} \rightarrow \mathrm{IIM'} - \mathrm{L} + \mathrm{IIZ} - \mathrm{ML_{z-1}}.$$

In *dissociation* (Figıre 2.3), the reactant molecule is dissociated on reactive *M*−*Z* sites on the surface. Similar to ligand exchange, dissociation may continue on the surface; but, it does not affect the number of bonded M atoms and the number of bonded ligands.

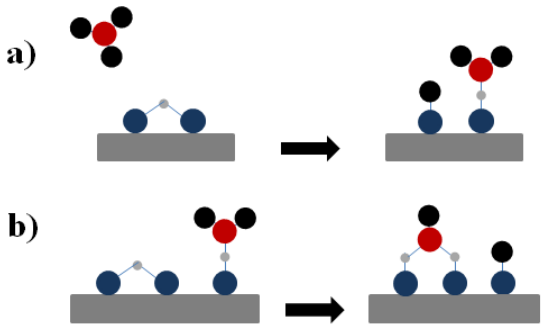

Figure 2.3: (a) Dissociation of the ML_z in surface M-Z sites. (b) Dissociation may also occur between MZ_{z-y} complex and M-Z sites.

iii) Association

$$II + ML_{z(g)} \rightarrow II...ML_z$$

In *association* (Figure 2.4), conception occurs without releasing the legends. Instead, reactant molecules form coordinative bonds with reactive surface sites.

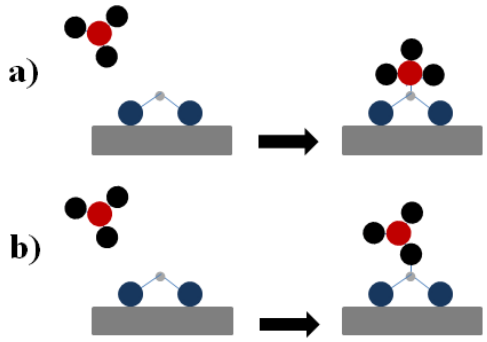

Figure 2.4: Association of the ML_z complex onto the surface. (a) Association can occur through formation of a coordinative bond between the central M ion and the surface, (b) or perhaps between the ligands and the surface.

From all these three chemisorption mechanisms, ligand exchange is preferred because its equilibrium condition can be satisfied by removing the gaseous byproducts.

When one cycle is completed, a certain amount of material is deposited on the surface, which is named as *growth per cycle* (GPC). GPC value is often less than a monolayer per cycle. The highest GPC values are obtained when the maximum number of surface sites react through ligand exchange, thereby releasing the maximum number of ligands into the gas phase, and reaction continues until steric hindrance terminates it. Although a certain number reactive sites are still available on the surface, ligands may block the bonding sites and the surface can be considered as full due to steric hindrance. Another reason of sub-monolayer saturation is the limited number of reactive sites, in which the number of bonding sites is less than required to achieve a full ligand coverage.

2.1.2 ALD Window

ALD window is the temperature range in which self-limiting growth occurs. Deposition in this range has an ideal constant growth rate of one monolayer per cycle. Center line in Figure 2.5 indicates the ALD window on the growth rate vs. temperature graph. There are some deviations from the ideal center line, representing the different mechanisms that prevent ALD process to fulfill the requirement of self-terminating reactions. At growth temperatures below the ALD window, deposition rate can be too high due to the condensation of precursor molecules on the substrate surface. In addition, at lower temperatures, due to lower reaction rates and slower mass transport, reactions might not be completed resulting in lower GPC values. At higher deposition temperatures, the most common case is thermal decomposition, in which surface controlled self-limiting mechanism is prevented by the gas-phase decomposition of precursor molecules. For this condition, a CVD-like growth mechanism is observed, in which GPC increases with temperature. On the other hand, declining deposition rates at higher temperatures might be indicating that monolayer desorption from the surface becomes the dominant surface process.

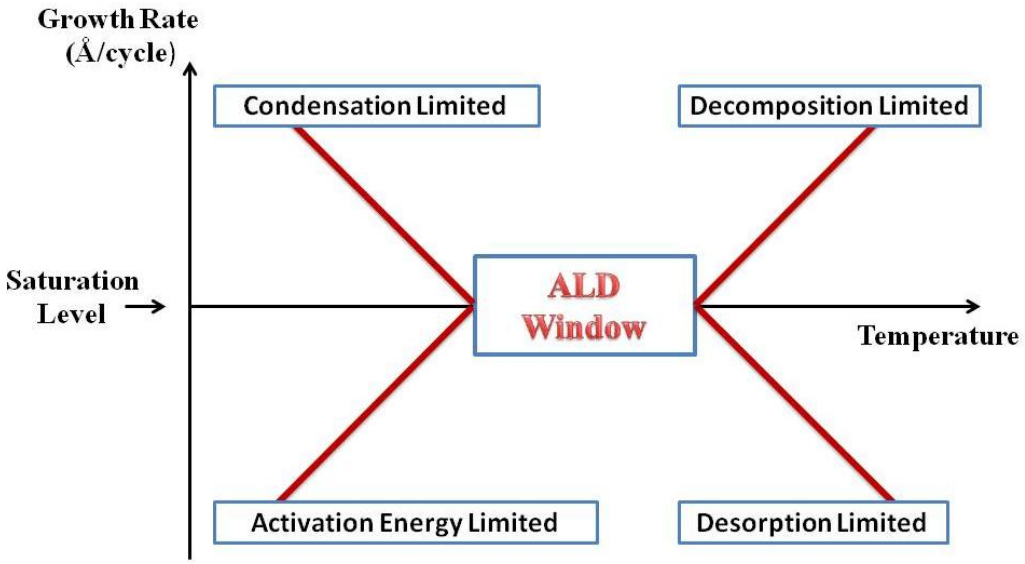

Figure 2.5: Effect of deposition temperature on the ALD growth rate.

2.1.3 Advantages and Disadvantages

Self-limiting surface reactions are the main characteristics of ALD. This kind of a growth mechanism comes with several advantages, such as:

- Simple and accurate thickness control by changing the number of reaction cycles,
- Excellent conformality and uniformity,
- Atomic level control of material composition,
- High quality material deposition at low processing temperatures,
- No need of reactant flux homogenity, which enables large area and batch capability,
- Good reproducibilty and straightforward scale-up,
- No gas phase reactions occur, favoring the usage of precursors that are highly reactive towards each other,
- Capability to prepare multilayer structures in a continuous process.

Disadvantages of the ALD method, on the other hand, are slow growth rate and low precursor utilization efficiency. However, these disadvantages can be compensated by proper adjustment of reactor design and precursor selection. A brief comparison of the ALD with other deposition methods is given in Table 2.1.

Table 2.1: Comparison of ALD with other thin film deposition techniques.[8]

Method	ALD	CVD	MBE	Sputter.	Evapor.	PLD
Thickness Uniformity	good	good	fair	good	fair	fair
Film Density	good	good	good	good	good	good
Step Coverage	good	varies	poor	poor	poor	poor
Interface Quality	good	varies	good	poor	fair	varies
Low Temp. Deposition	good	varies	good	good	good	good
Deposition Rate	poor	good	fair	good	good	good
Lack of Pinholes	good	good	good	fair	fair	fair
Automated Multilayers	good	fair	good	good	fair	fair
Industrial Applicability	varies	good	varies	good	good	poor
MBE = Molecular Beam Epitaxy		CVD = Chemical Vapor Deposition				
PLD = Pulsed Laser Deposition						

2.1.4 Precursors

The selection of precursors for an ALD process necessitates some criteria to be taken into consideration. Precursors might be gases, volatile liquids or solids. However, the vapor pressure must be high enough to enable effective mass transport, which requires the heating of all solid and some liquid precursors. Besides sufficient volatility, precursors must be thermally stable at the substrate temperature to avoid self-decomposition. Decomposition of the precursor results in uncontrolled gas-phase reactions which eliminates the self-limiting growth mechanism and the related advantages. Other requirements include aggressive and complete reactions, no etching of or dissolution into film or the substrate, unreactive volatile byproducts and sufficient purity. All basic CVD precursor

requirements also apply, such as reasonable cost, easy synthesis and handling, and environmental friendliness [9].

Typical precursors used in ALD are halides (especially chlorides), alkyl compounds and alkoxides. Thermodynamic calculations are useful in predicting the feasibility of the reaction; but, the data in literature are not enough especially for organometallic compounds, such as cyclopentadienyl complexes and alkyl and silyl amides. The common non-metal precursors used in ALD processes are: water (H_2O), oxygen ($O_{2)}$, ozone (O_3), alcohols (ROH), hydrogen peroxide (H_2O_2), atomic oxygen created from plasma as the O_2, ammonia (NH_3) or nitrogen/ammonia (N_2/NH_3) plasma (or, less often, N_2, NH_3+catalyst, RNH_2, N_2H_4, R_2NNH_2) as the nitrogen, H_2S as the sulphide, H_2Se as the selenide, Te or MeAyTe as the telluride source [3].

2.1.5 Plasma vs. Thermal ALD

In order to enable exchange reactions between the precursor molecules and surface species, an activation energy is required. In thermal ALD, which is the conventional mode of ALD, this energy is provided thermally, only by heating the substrate or the entire reactor chamber. Plasma-enhanced ALD (PEALD) (also called as plasma-assisted ALD, PAALD) is the most widely used technique as an alternative to thermal ALD. In PEALD, the plasma source creates ions and radicals, which enhance the chemical reactions towards the film growth.

In PEALD, due to the enhancement of chemical reactions, wider range of materials can be deposited at low temperatures, which gives opportunity for the use of temperature sensitive substrates. PEALD enables shorter deposition times (higher growth rates), which increase the throughput and make it more attractive for mass production. Although the use of plasma enables further

utilization of material and precursor properties, substrate temperature and process conditions, it might also result in reduced conformality and potential plasma damage.

Compared to thermal ALD, the PEALD chamber configuration is more complicated. There are three main reactor configurations for PEALD depending on the position of the plasma source, namely, radical-enhanced, direct, and remote plasma systems (Figure 2.6).

Radical-enhanced ALD is the first ALD reactor configuration (Figure 2.6(a)), which is a modified version of a thermal reactor with a plasma generator. Plasma generation takes place at a relatively far distance from the substrate surface. Therefore, surface collisions occur, in which ions and electrons recombine and lost before reaching the substrate. In order to increase the efficiency of this configuration, radicals with a low surface recombination probability or very long radical exposure times are needed to reach saturation of the reactants.

In direct plasma configuration (Figure 2.6(b)), a capacitively-coupled plasma is generated at radio frequency (RF, 13.56 MHz) between two parallel electrodes, one of which is powered, while the other one is grounded under the substrate. Because plasma is generated very close to the substrate surface, the fluxes of plasma radicals and ions are very high. As a result, uniform deposition over high wafer areas with short exposure times are observed, which makes this configuration very preferable for industrial applications. However, processing conditions must be carefully optimized in order to avoid plasma damage resulting from the emission of high energy photons.

In remote plasma ALD (Figure 2.6(c)), neither plasma is generated outside the chamber nor the substrate is involved in plasma generation. In this case, plasma source is located remotely from the substrate holder. This configuration

has significant advantages over other plasma system designs. Due to the generation of "downstream" plasma, the flux of the radicals is much higher than that in radical-enhanced ALD. In addition, plasma and substrate conditions can be controlled easily and independently, which is not possible for direct plasma ALD [11].

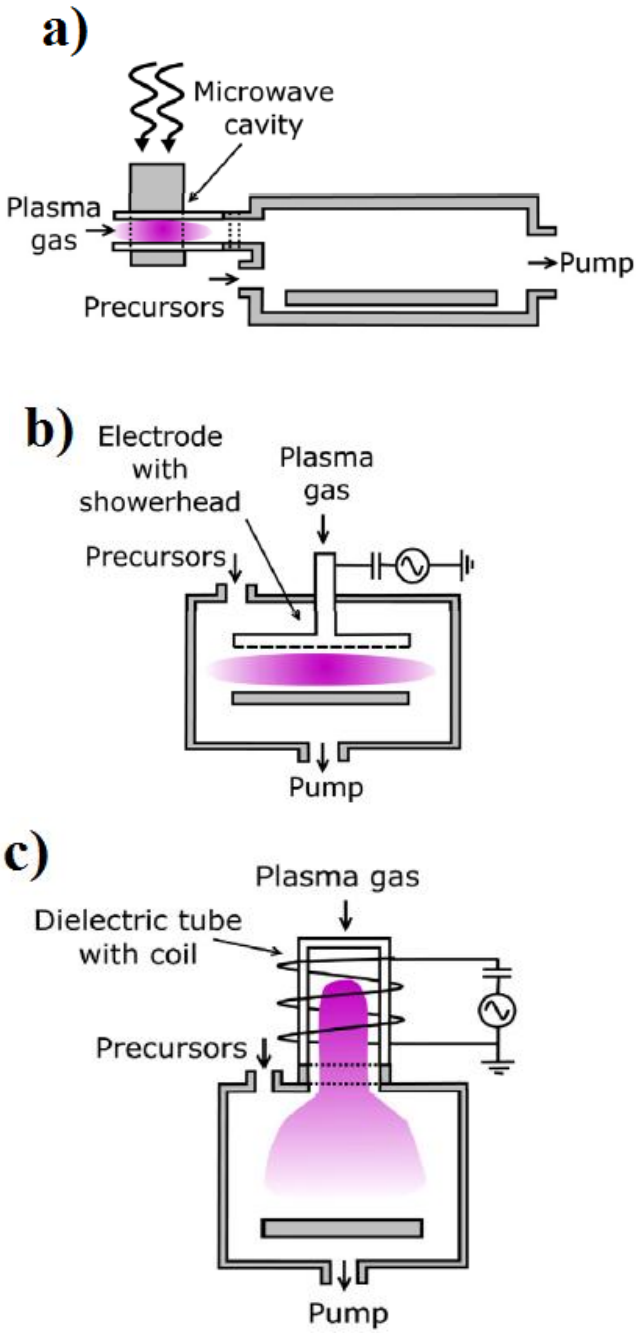

Figure 2.6: Three main types of plasma reactor configurations for PEALD. (a) Radical-enhanced, (b) direct plasma, and (c) remote plasma configurations [10]

Several plasma sources can be used in remote-plasma ALD systems, such as electron cyclotron resonance (ECR) plasma, microwave plasma, and RF-driven inductively-coupled plasma (ICP). The plasma system used in this thesis study is a remote-plasma ALD system with RF-driven ICP plasma source. In addition, thermal ALD system is used for the synthesis of nanotubes.

2.2 Ga_2O_3 Deposition Using PEALD

Ga_2O_3 is a wide band gap material with good thermal and chemical stability, high dielectric constant, and wide band gap (~4.9 eV) [12, 13]. Combination of these properties enables Ga_2O_3 thin films to be used in various applications, including solar cells [14], gas sensors [15], deep-UV photodetectors [16], field-effect transistors [17], and spintronics [18].

The growth of Ga_2O_3 films has been accomplished by several techniques, such as magnetron sputtering [19], electron beam evaporation [20], pulsed laser deposition [21], molecular beam epitaxy [22], metal-organic chemical vapor deposition (MOCVD) [23], vapor phase epitaxy [24], and sol-gel process [25].

Several studies have been reported for the ALD of Ga_2O_3 thin films using different precursors. First report on the PEALD of Ga_2O_3 using O_2 plasma was published by Shan et al. [14]. Their study, in which $[(CH_3)_2GaNH_2]_3$ was used as the gallium (Ga) precursor, presented the structural, electrical and optical properties of the deposited films [26, 27]. Ga_2O_3 and mixed Ga_2O_3-TiO_2 films have also been grown by PEALD using $[(CH_3)_2GaNH_2]_3$ and $Ti(NMe_2)_4$ precursors in order to obtain films with high dielectric constant and low leakage current for electronic device applications [12, 28, 29]. Another study is about the fabrication of metal-insulator-semiconductor capacitors using Ga_2O_3 as the insulating layer [30]. Ga precursor used in this study was not mentioned by the authors. Besides PEALD, few studies regarding the growth of Ga_2O_3 films using

thermal ALD were reported as well. Dezelah et al. [31] employed $Ga_2(NMe_2)_6$ together with H_2O to obtain Ga_2O_3 thin films. This process exhibited an ALD window between 170 and 250 °C with a growth rate of 1 Å/cycle. Recently, Lee et al. [32] reported on the deposition of Ga_2O_3 thin films via both ALD and MOCVD using a new Ga precursor, dimethylgallium isopropoxide ($Me_2GaOiPr$). A narrow ALD window (280–300 °C) was reported for the process and growth rate was found to be 0.28 Å/cycle in this temperature regime.

2.3 In_2O_3 Deposition Using PEALD

In_2O_3 has attracted a considerable amount of interest for a variety of applications in micro-electronics and optoelectronics. It has a wide band gap (~3.7 eV) and behaves like an insulator in its stoichiometric form, while in its non-stochiometric form (In_2O_x), it appears to have n-type semiconducting properties [33]. It is commonly doped with tin oxide (SnO_2) to form indium tin oxide (ITO), which has an excellent combination of high optical transmission (transparency) and high electrical conductivity [34].

Deposition of In_2O_3 using ALD has reported by several groups with a number of precursors. A variety of precursors have investigated for the deposition of In_2O_3. Zr-doped In_2O_3 and ZrO_2-In_2O_3 thin layers were deposited using $InCl_3$ and In(thd)3 (thd = 2,2,6,6-tetramethylheptane-3,5-dionate) as the indium precursors [35,36]. $InCl_3$ was also used together with water (H_2O) and hydrogen peroxide (H_2O_2) to deposited In_2O_3 and Sn-doped In_2O_3 (ITO) [37]. Another precursor used for the deposition of In_2O_3 was trimethylindium (TMIn) [38]. Nilsen et al, on the other hand, used $In(acac)_3$ (acac = acetylacetonate, pentane-2,4-dione) and either H_2O or O_3 as precursors [39].

In addition, cyclopentadienyl indium (CpIn) and ozone (O_3) have been used previously to grow indium oxide and ITO [40]. In 2006, CpIn was first used by Elam et al [41], together with O_3 as the oxygen source. However, they observed that thermal decomposition of ozone prevents them from coating high aspect ratio nanostructures with high conformality. In addition, minimum activation temperature of O_3 was 200 °C, which disabled the usage of temperature sensitive substrates such as polymers. Therefore, using the same indium precursor (CpIn), they deposited In_2O_3 films using the combination of H_2O and O_2 as the oxygen source [42]. In this study, efforts on the deposition of In_2O_3 films using CpIn and O_2 plasma as the indium and oxygen sources are presented.

2.4 Fabrication of Tubular Nanostructures Using ALD

Besides conventional thin film deposition on planar surfaces and substrates, ALD has also been effectively used for synthesis of various nanostructures such as nanoparticles and nanotubes through template-based deposition routes. Due to its conformal deposition capability at low temperatures, a wide selection of materials has been used as nanostructured templates for ALD growth. Among these, anodic aluminum oxide (AAO) is the most widely reported template, which was generally used for the synthesis of oxide nanotubes by ALD [43-47]. Elemental/compound semiconductors and carbon nanotube templates have been used as well for synthesis of hollow nanostructures [48, 49]. Several groups have used electrospun polymeric nanofibers as templates to fabricate nanotubes of Al_2O_3 [50, 51], SnO_2 [52], TiO_2 [53-55] and ZnO [50, 56-58] using ALD. In these studies, electrospun nanofibers of poly(vinyl alcohol) [50, 51], polyacrylonitrile [52], poly(vinyl pyrrolidone) [53, 54], and poly(vinyl acetate) [55, 58] were used as polymeric nanofiber templates.

Nanotubes of oxide materials exhibit attractive electrical properties and thus have potential applications in microelectronics. Among these materials, HfO_2 has attracted significant interest due to its high thermal and mechanical stability, chemical inertness, rather large band gap (~5.8 eV), high dielectric constant and refractive index, as well as good transparency in the visible spectral range and low photon energies [59, 60]. Several different templates were reported to be used for the fabrication of HfO_2 nanotubes via ALD. HfO_2 nanotubes obtained using AAO templates were studied by several groups [61-63]. Similar structures were fabricated by deposition of a conformal HfO_2 layer on porous silicon templates [64]. In 2009, Shandalov et al. [65] studied the size dependent polymorphism of HfO_2 nanotubes using Ge (111) nanowire arrays as templates. Recently, carbon nanotubes were coated with HfO_2 using ALD in order to study the field emission properties of the designed structure [66]. However, to the best of our knowledge, fabrication of HfO_2 nanotubes by combining electrospinning and ALD has not been reported yet.

Chapter 3

Experimental Details

This chapter provides a detailed explanation of thin film deposition parameters, characterization tools and metal-oxide-semiconductor (MOS) capacitor fabrication process steps. All of the deposition and fabrication processes were conducted at UNAM Cleanroom Facility (UCF).

3.1 Ga_2O_3 deposition using PEALD

Ga_2O_3 thin films were deposited on silicon (Si) (111) wafers. Substrate cleaning procedure started with 5 minutes sequential ultrasonic agitation in isopropanol, acetone, methanol, and de-ionized (DI) water. After that, the samples were treated in (1:19) HF: H_2O mixture for 1 min to remove native oxide on substrate surface. As the last step of the cleaning procedure, Si (111) wafer pieces were rinsed with DI water and dried using nitrogen (N_2) gun.

Deposition experiments were carried out using a Fiji F200 LL ALD reactor (Cambridge Nanotech Inc.) equipped with a load lock. The Fiji is a modular high-vacuum ALD system that is capable of doing thermal as well as plasma-enhanced depositions. The details of the system are presented in Figures 3.1 and 3.2.

Figure 3.1: Fiji F200 LL plasma-enhanced atomic layer deposition system, which was used for the Ga_2O_3 depositions.

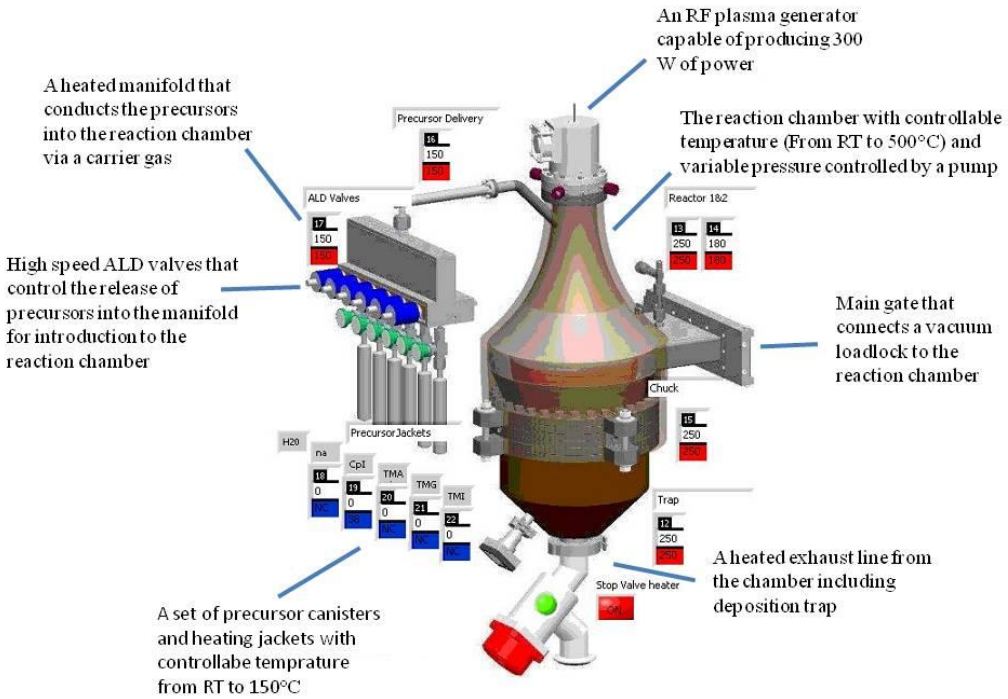

Figure 3.2: Details regarding to the main components of Fiji F200 LL remote-plasma ALD system.

Ga_2O_3 thin film depositions were carried out by alternating exposures of TMG ($Ga(CH_3)_3$) and O_2 plasma. Using these precursors, Ga_2O_3 thin films were

deposited at temperatures starting from room temperature to 400 °C. Due to its high vapor pressure, TMG bottle was cooled down to ~ 6 °C using a home-made Peltier system. Ar was used as the carrier gas with the flow rates of 60 and 200 sccm for TMG and O_2 plasma, respectively. Base pressure of the system was ~ 0.20 Torr. For the optimization of growth parameters, 150 cycles were deposited at 250 °C, where 1 cycle consisted of 0.015 s TMG (~6 °C)/5 s Ar purge/2–60 s (25 sccm, 300 W) O_2 plasma/5 s of Ar purge. In Figure 3.3, optimized recipe and the pressure data are presented. This recipe was used with different number of cycles for the characterization of samples. Post-growth annealing of Ga_2O_3 films was performed at temperatures ranging rom 500 to 1000 °C using a rapid thermal annealing system under 100 sccm N_2 flow with the heating rate of 10 °C/sec.

	Instruction	#	Value	
0	flow	0	20	Flow carrier gas 0 (Ar) with 20 sccm
1	flow	1	20	Flow carrier gas 1(Ar) with 200 sccm
2	flow	2	0	Flow reactant gas 2 (N_2) at 0 sccm
3	wait		1200	Wait 1200 s
4	MFCvalve	3	1	Open MFCvalve (O_2 plasma)
5	flow	0	60	Increase carrier gas 0 flow to 60 sccm
6	flow	1	200	Increase carrier gas 1 flow to 200 sccm
7	flow	2	0	Flow reactant gas 2 (N_2) at 0 sccm
8	flow	3	0	Flow carrier gas 3(O_2) at 0 sccm
9	wait		30	Wait 30 s
10	pulse	4	0.015	Open valve 4 (TMG) for 0.015 seconds
11	wait		5	Wait 5 s for purging via carrier gas
12	plasma		300	Set plasma power to 300 W
13	wait		1	Wait 1 s
14	flow	3	25	Flow reactant gas 3 (O_2 plasma) with 25 sccm
15	wait		20	Wait 20 s
16	flow	3	0	Flow reactant gas (O_2 plasma) at 0 sccm
17	plasma		0	Turn off plasma power
18	wait		5	Wait 5 s for purging
19	goto	10	800	Go to step 10 and repeat steps 10-19 for 800 times
20	MFCvalve	3	0	Turn off MFC 3
21	flow	0	20	Reduce carrier gas 0 (Ar) flow to 20 sccm
22	flow	1	20	Reduce carrier gas 1 (Ar) flow to 20 sccm

* Heater 12 (Trap), 13 (Reactor 1), 14 (Reactor 2) and 15 (Chuck) were set to 250 °C and stabilized before depositions

Figure 3.3: Optimized PEALD recipe for the growth of Ga_2O_3 with 800 deposition cycles. The table on the left shows the constructed recipe by using the Fiji F200 LL's software. The description of the comments is given on the right hand side of the figure.

3.2 In_2O_3 deposition using PEALD

In_2O_3 thin films were grown on solvent-cleaned Si(111) substrates at 150 and 250 °C in Fiji F200 LL PEALD system equipped with a load lock. Films were deposited using the alternating exposures of CpIn and O_2 plasma. Plasma power was set to 300 W and Ar was used as a carrier and purging gas with the flow rates of 60 and 200 sccm for CpIn and O_2 plasma, respectively. Purge time was kept constant at 5 s and the base pressure of the system was ~0.20 Torr. Due to its low vapor pressure, CpIn was heated to 85 °C prior to depositions. For the optimization of growth parameters, 100 ALD cycles were deposited at 150 °C.

3.3 Metal-Oxide-Semiconductor Fabrication

Metal-oxide-semiconductor (MOS) capacitor is a two-terminal device consisting of a semiconductor body or substrate, an insulating oxide and a metal electrode called a gate. In order to perform electrical characterization on the deposited films, metal/oxide/semiconductor devices were fabricated using the ALD-grown Ga_2O_3 as the insulating oxide layer. Schematic representation of the fabrication steps is given in Figure 3.4.

All of the fabrication processes were conducted at UNAM laboratories, class 100 and 1000 cleanroom facilities (UNAM Cleanroom Facility-UCF).

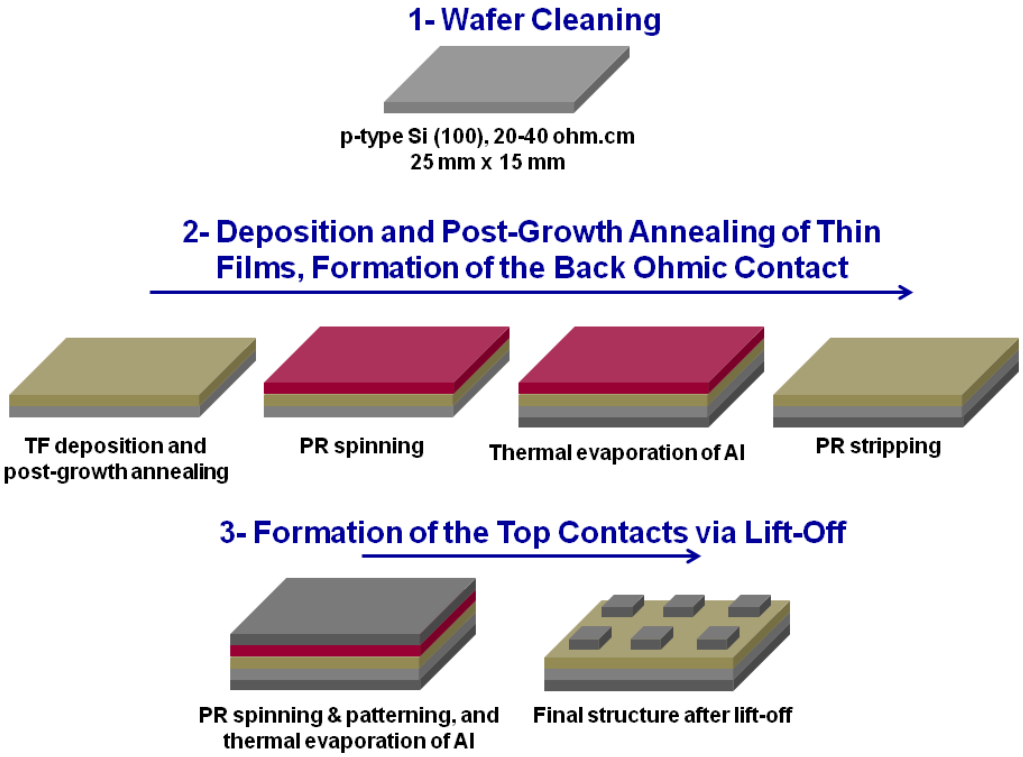

Figure 3.4: Schematic of the fabrication steps for metal/oxide/semiconductor devices.

3.3.1 Substrate and Surface Preparation

4 inch p-type Si (100) wafers (ρ = 20-40 ohm.cm) were used for the fabrication of MOS capacitors. These wafers were cleaved to 25 mm x 15 mm pieces using a dicer machine (Disco, DAD3220). 10 mm x 20 mm mask size was used along the device fabrication. Three Si pieces were used for each Ga_2O_3 deposition, which were then annealed at 700, 800, 900, and 1000 °C.

Cleaning of the surface at the beginning and after each fabrication step is very critical for the performance of the resulting devices and repeatability of the measurement. For Si wafers, it is ideal to start with the standard RCA (Radio Corporation of America) cleaning. In this cleaning procedure, large residues were cleaned with acetone, methanol, isopropyl alcohol, and DI water.

Afterwards, samples were immersed into Piranha solution (H_2SO_4: H_2O_2 with 4:1 volume ratio), and kept in this solution for 15 minutes. Last step of the cleaning procedure is the native oxide etching in (1:50) HF:H_2O mixture for a few minutes. After each step, samples were rinsed in DI water and dried by blowing N_2.

3.3.2 Deposition and Post-growth Annealing of Ga_2O_3 Thin Films

Si wafers were loaded into Fiji F200 LL ALD system (Cambridge Nanotech Inc.) immediately after the cleaning operation. 120, 800 and 1200 cycles of Ga_2O_3 were deposited at 250 °C to study the effect of film thickness on electrical device characteristics. Details regarding to the growth parameters are given in Chapter 2. For each deposition, 4-5 Si pieces were loaded into the chamber. After the depositions, these pieces were annealed at four different temperatures (700, 800, 900, and 1000 °C) for 30 minutes under 100 sccm N_2 flow using ATV–Unitherm (RTA SRO-704) rapid thermal annealing system (Figure 3.5). Using these samples, effects of both film thickness and post-growth annealing temperature on the dielectric characteristics of Ga_2O_3 were studied.

For the samples prepared by the deposition of 1200 Ga_2O_3 PEALD cycles, a 5 nm-thick Al_2O_3 layer was immediately coated on the Ga_2O_3 films after the annealing process. Savannah S 100 thermal ALD system was used for the Al_2O_3 depositions. Fifty cycles of Al_2O_3 were deposited using the Cambridge Nanotech Inc's standard recipe for trimethylaluminum (TMAl) and water (H_2O) process at 200 °C.

Figure 3.5: ATV – Unitherm rapid thermal annealing system (RTA SRO-704).

3.3.3 Preparation of Back Ohmic Contact

Back-contact metallization was carried out by the thermal evaporation of a ~80 nm-thick aluminum (Al) layer using VAKSIS Thermal Evaporation system (PVD Vapor – 3S Thermal) (Figure 3.6). For protective purposes, front sides of the samples were coated with a layer of photoresist before metallization. Standard AZ5214E of AZ Electronic Materials was spin coated at 4000 rpm for 50 seconds, which was followed by the standard photoresist bake at 110 °C for 50 seconds.

Figure 3.6: VAKSIS (PVD Vapor – 3S Thermal) thermal evaporation system.

After metallization, photoresist layer was stripped by rinsing the samples in acetone, methanol, isopropanol, and DI water. After drying with N_2, samples were ready for ohmic contact formation. P-type ohmic contact formation step is required for reliable MOS devices, since work functions of Al and Si are different from each other. For this purpose, samples were annealed in ATV RTA system at 450 °C for 2 minutes under N_2 atmosphere.

3.3.4 Photolithography and Development

As the next step of the fabrication process, photolithography was applied in order to transfer the desired patterns onto samples. This process was carried out in the UCF lithography room. Before starting photolithography, samples were once-again cleaned using the RCA process and then baked at 120 °C for 5 minutes to remove humidity off the surface and to obtain better adhesion of the photoresist layer to the substrate surface. Adhesion promoter, hexametyldisilazane (HMDS) was spin coated with 5000 rpm for 50 seconds. Then, AZ5214E positive tone photoresist was spin-coated at 4000 rpm for 40

seconds (Figure 3.7(a)), resulting in ~1.4 μm resist thickness. This was followed by a post-exposure bake, which was applied at 110 °C for 50 seconds.

Electronic Vision Group EVG620 Mask Aligner was used for exposing photoresist layer to UV with a constant dose of 40 mJ (Figure 3.7(b)). Post-exposure bake was used to further improve resolution, but this step was skipped, since the minimum feature size in this work was not within the critical range and the lithography resolution was repeatable without this step. After the UV exposure, regions that were subjected to UV light become soluble in the developer solution. AZ400K developer (AZ400K:H_20 with 1:4 volume ratio) was used for the development of exposed samples. Development time could be observed during the etching of the soluble photoresist by color change. For this process 20 s of development time was found to be ideal. After development, samples were immediately rinsed in DI water and dried using N_2 gun. In order to check whether the desired structures were obtained, an optical microscope was used.

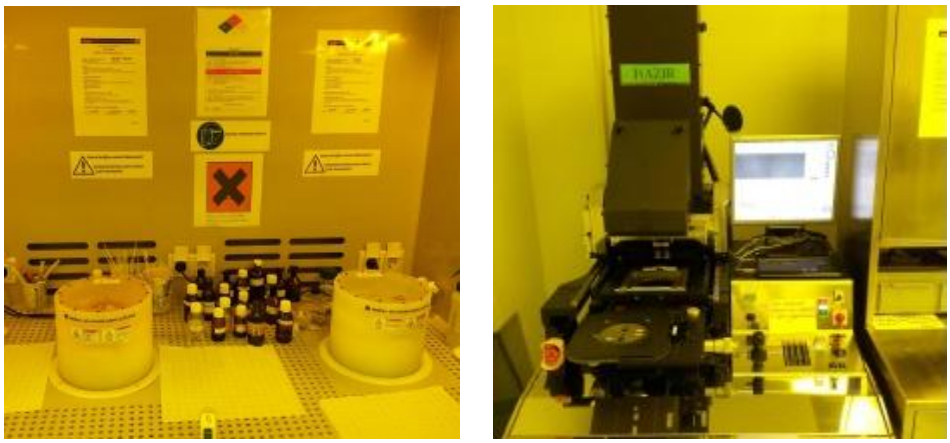

Figure 3.7: (a) Hexametyldisilazane and AZ5214E photoresist were spin coated on top of the samples by using Laurell spinner system. (b) Electronic Vision Group EVG620 Mask Aligner used for the alignment and exposure of photoresist coated samples.

3.3.5 Metallization and Lift-Off

For the formation of top contacts, ~ 80 nm-thick Al was evaporated on patterned samples using the VAKSIS Thermal Evaporation system. As the next step, samples were left in acetone for a few hours in order to dissolve photoresist (i.e lift-off process). If needed, additional sonification was done for a faster and complete dissolution of the photoresist and hence the metal layer on top of it. After the lift-off process, samples were rinsed in isopropanol and DI water, then dried using N_2 gun. As a result, region that was subjected to UV exposure remained as Al top contact. Both the mask and the resulting device structure are shown in Figure 3.8.

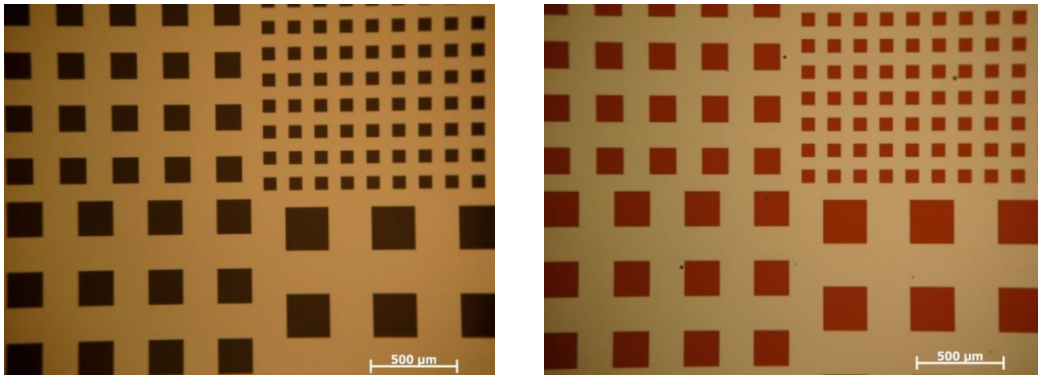

Figure 3.8: Optical microscopy images of (a) the photomask, and (b) the resulting structure with 75, 150, 200, and 250 µm wide square Al contact pads.

3.4 Synthesis of HfO_2 Nanotubes Using Electrospinning and ALD

Nylon 6,6 nanofibers having different average fiber diameters were obtained by electrospinning. Polymer solutions were prepared by dissolving 5% (w/v) nylon 6,6 in 1,1,1,3,3,3-hexafluoro-2-propanol (HFIP) (Sigma-Aldrich, ≥ 99%) and 8% (w/v) nylon 6,6 in formic acid (Sigma-Aldrich, 98-100%). Prepared solutions were stirred for 3 h at room temperature. Viscosities of the nylon 6,6

solutions were measured using Anton Paar Physica MCR-301 Rheometer equipped with cone/plate accessory using the spindle type CP40-2 at 22 ^{o}C and a constant shear rate of 100 s^{-1}. Homogeneous nylon 6,6 solutions were then placed in 3 ml syringes fitted with metallic needles of 0.8 mm inner diameter. Syringes were fixed horizontally on the syringe pump (Model: SP 101IZ, WPI). Polymer solutions were pumped with a feed rate of 1 ml/h during electrospinning. 15 kV was applied to the metal needle tip using a high voltage power supply (Matsusada, AU Series). Tip-to-collector distance was set at 10 cm. Way to the grounded stationary cylindrical metal collector (height: 15 cm, diameter: 9 cm), solvents were evaporated and nylon 6,6 nanofibers were deposited on an aluminum foil covering the collector. Electrospinning processes were carried out at 23 °C and 36% relative humidity in an enclosed Plexiglas box. Figure 3.9(a) shows the schematic representation of the electrospinning process.

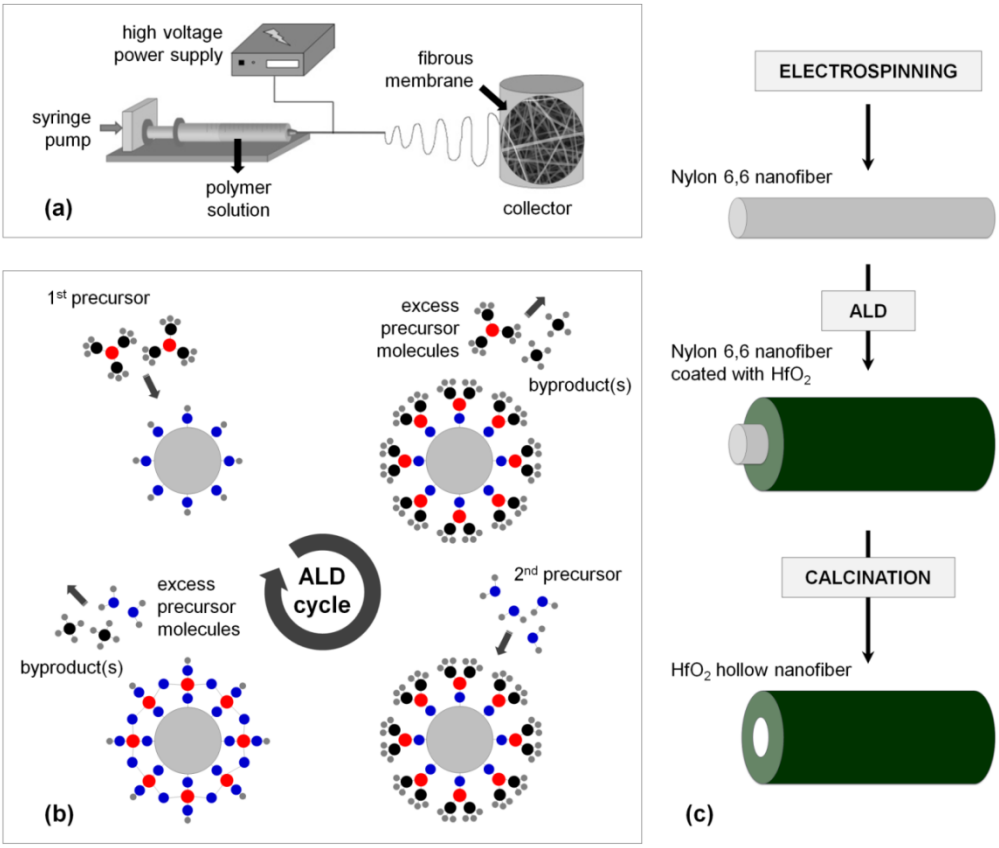

Figure 3.9: Schematic representations of (a) electrospinning and (b) ALD processes. (c) Schematics of the combined process used to fabricate HfO_2 nanotubes.

Following the fabrication of nylon 6,6 nanofibers by electrospinning, these polymeric templates were introduced into the thermal ALD system (Savannah S100 ALD reactor, Cambridge Nanotech Inc.) (Figure 3.10) and coated with HfO_2. Depositions were performed using tetrakisdimethylamidohafnium (TDMAH, $Hf(NMe_2)_4$) and H_2O as the organometallic precursor and oxidant at 200 °C. (Figure 3.9(b)). $Hf(NMe_2)_4$ was preheated to 75 °C and stabilized at this temperature before the depositions, which were carried out at a base pressure of 0.25 Torr using N_2 as the carrier gas with a flow rate of 20 sccm. Pulse times of the precursor and oxidant were 0.2 and 0.015 s, which were followed by 15 and 10 s purge periods, respectively. Using this recipe, 200 cycles HfO_2 was also deposited on a solvent-cleaned planar Si (100) substrate at 200 °C. Thickness of the HfO_2 layer was measured by spectroscopic ellipsometry as 22 nm, corresponding to a deposition rate of 1.1 Å/cycle.

Figure 3.10: Savannah S100 thermal ALD reactor (Cambridge Nanotech Inc.) used for the deposition of HfO_2 on electrospun nylon nanofibers.

An additional deposition was also carried out using the exposure mode (a trademark of Cambridge Nanotech Inc.), in which dynamic vacuum is switched to static vacuum just before the precursor and oxidant pulses and switched back

to dynamic vacuum before the purging periods after waiting for an additional time, allowing precursor and oxidant molecules to diffuse into the high-density and high-surface area nanofiber template. Regardless of the deposition mode, 600 ALD cycles were applied. After the depositions, calcination process was performed at 500 °C for 2 h under atmospheric conditions in order to remove the polymeric cores of the nanofibers (Figure 3.9(c)).

3.5 Characterization Methods

3.5.1 Scanning Electron Microscopy

The scanning electron microscope (SEM) uses a focused beam of high-energy electrons to generate a variety of signals that derive from electron-sample interactions at the surface of specimens. These signals include secondary electrons (that produce SEM images, mainly used for morphology and topography studies), backscattered electrons (effective in rapid phase discrimination due to composition contrast), diffracted backscattered electrons (that are used to determine crystal structures and orientations), photons (characteristic X-rays that are used for elemental analysis), visible light (cathodoluminescence), and heat. SEM has many advantages over optical microscopes, including large depth of field and much higher resolution. In addition, because the SEM uses electromagnets rather than lenses, one has much better control in imaging parameters such as focus, magnification, and astigmatism, which all affect the final image quality.

Nova NanoSEM scanning electron microscope (SEM) (FEI) (Figure 3.11) was used to reveal morphology, uniformity and dimensions of the samples. Prior to imaging, HfO_2 samples were coated with 5 nm Au/Pd to eliminate the charging effect.

Figure 3.11: Nova NanoSEM scanning electron Microscope used for the surface imaging of Ga_2O_3 thin films and HfO_2 nanostructures.

3.5.2 Atomic Force Microscopy

Atomic force microscopy (AFM) is a very high resolution type of scanning probe microscopy (SPM) with high sensitivity that penetrates the regime of interatomic forces between single atoms. AFM images are obtained by measurement of the force created by the proximity to the surface of the sample on a sharp tip at the end of the cantilever [67]. Forces between the tip and the sample lead to a deflection of the cantilever according to Hooke's law from which the interaction between the tip and sample can be found. AFM has the advantage of imaging almost any type of surface, including polymers, ceramics, composites, glass, and biological samples. The dominant interactions at short probe-sample distances in the AFM are Van der Waals (VdW) interactions. However, long-range interactions (i.e. capillary, electrostatic, magnetic) are significant further away from the surface. These are important in other SPM methods of surface analysis.

In this work, surface morphologies and root-mean square (RMS) roughnesses of the thin films were investigated using an Asylum Research, MFP-3D instrument in contact mode (Figure 3.12).

Figure 3.12: Asylum Research MFP-3D AFM used for the morphological characterization of Ga_2O_3 thin films.

3.5.3 X-Ray Photoelectron Spectroscopy

X-Ray photoelectron spectroscopy (XPS) is a widely used analytical technique for the investigation of chemical composition of solid surfaces. In addition, several other significant thin film materials information can be obtained using XPS, such as chemical states, spatial distribution in three dimensions, film thickness and uniformity.

The parts of XPS system are: the sample under investigation, a source of primary radiation and an electron energy analyzer, which are all under ultra-high vacuum regime. Analysis is accomplished by irradiating a sample with mono-energetic soft X-rays and energy analysis of the electrons emitted. Photons interact with the atoms at the surface of the sample by photoelectric effect, which causes the surface electrons to be emitted. Binding energies of the emitted electrons are given by:

$$E_B = hv - E_K - W \tag{3.1}$$

where hv is the photon energy, E_K is the kinetic energy of the electron, and W is the spectrometer work function. Using XPS, E_K is measured by the spectrometer, but is dependent on the photon energy of the X-rays employed. Since all three quantities at the right-hand side of the equation are either known or measurable, it becomes relatively straight-forward to calculate the binding energy of the electron. This calculation is performed by control electronics associated with the spectrometer.

In this work, Thermo Scientific K-Alpha spectrometer equipped with a monochromatized Al Kα X-ray Source was used (Figure 3.13). Sputter depth profiling was carried out with a beam of Ar ions having an acceleration voltage and spot size of 1 kV and 400 μm, respectively.

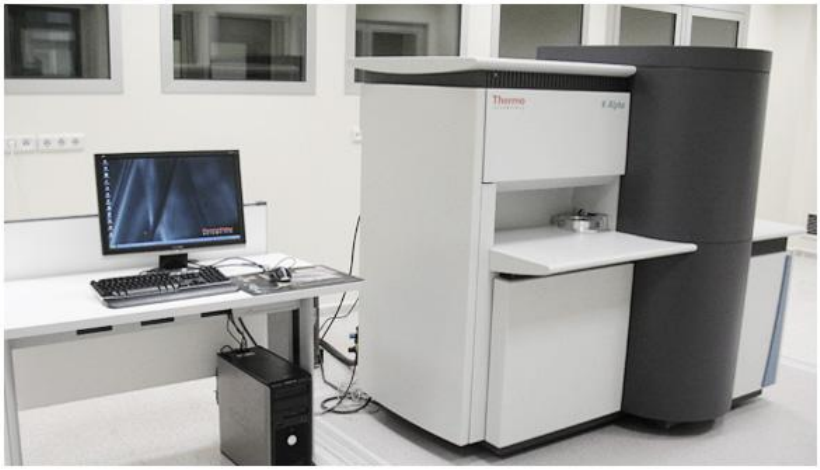

Figure 3.13: Thermo Scientific K-Alpha X-Ray photoelectron spectroscopy system located at UNAM Characterization Laboratories.

3.5.4 X-Ray Diffraction

X-ray diffraction (XRD) is a structural characterization technique primarily used for phase identification of a crystalline material and can provide information on unit cell dimensions. XRD is based on constructive interference of monochromatic X-rays and a crystalline sample. These X-rays are generated by

a cathode ray tube, filtered to produce monochromatic radiation, collimated to concentrate and then directed toward the sample. As a result of the interaction of the incident rays with the sample, constructive interference occurs. This condition is described by Bragg's Law:

$$n\lambda = 2d\ sin\theta \qquad (3.2)$$

where n is an integer, λ is the wavelength of the X-rays, d is the interatomic spacing of the layers and θ is the diffraction angle in degrees (Figure 3.14). By changing the angle, Bragg's Law conditions are satisfied by different *d*-spacings in polycrystalline materials. Plotting the angular positions and intensities of the resultant diffracted peaks of radiation produces a pattern, which is characteristic of the sample.

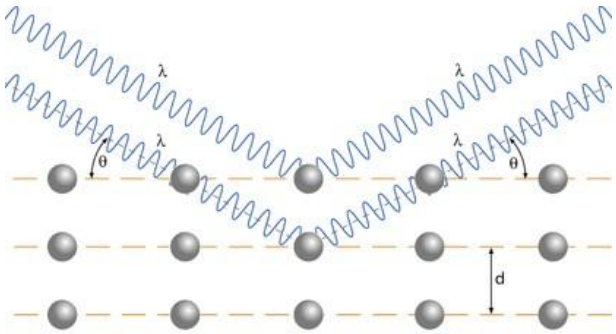

Figure 3.14: Schematic illustration of Bragg condition and Bragg's law [68]

Several information about the structural characteristics of the sample can be obtained from X-ray diffraction measurements, such as:

- phases present in the sample and quantitative phase analysis,
- crystal structure,
- unit cell lattice parameters,
- average crystallite size of nanocrystalline samples,
- crystallite microstrain,
- texture,
- residual stress.

In conventional XRD with large incident angles, an incident X-ray beam penetrates deep into a material. In order to obtain information from very thin layers, grazing-incidence XRD (GIXRD) is preferred. In GIXRD, a very small incidence angle is used, which enables the small penetration depths and intensity enhancement at the surface. During the collection of the diffraction spectrum, only the detector rotates through the angular range; therefore, the incident angle, the beam path length and the irradiated area are kept constant. As a result, GIXRD is used to analyze crystal structures ranging from a few to hundred nanometers below the surface of the solids. It allows phase analysis on very thin layers and surface sensitivity down to nm scale.

XRD measurements of polymer and HfO_2 samples were performed in PANalytical's X'Pert PRO Multi-Purpose X-Ray Diffractometer (XRD) operated at 45 kV and 40 mA, using Cu Kα radiation (λ = 0.15418 nm). For Ga_2O_3 and In_2O_3 thin films, grazing-incidence x-ray diffraction (GIXRD) measurements were performed in a PANanalytical X'Pert PRO MRD diffractometer operating at 45 kV and 40 mA, using Cu Ka radiation (Figure 3.15). Initial scans were performed within the range of 10°–90° using 0.1° step size and 0.5 s counting time. For the crystalline samples, additional data were obtained within the same 2h range by the summation of eight scans, which were performed using 0.1° step size and 10 s counting time.

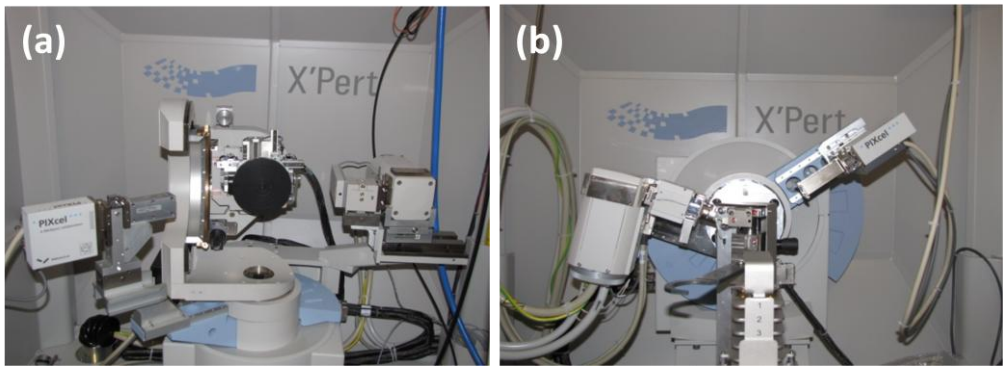

Figure 3.15: PANalytical's (a) X'Pert PRO Materials Research Diffractometer (b) X'Pert PRO Multi-Purpose X-Ray Diffractometer.

3.5.5 Transmission Electron Microscopy

Similar to SEM, transmission electron microscope (TEM) utilizes electrons as the imaging source and takes advantage of their significantly smaller wavelength, which makes it possible to get an imaging resolution of at least several orders of magnitude better than a conventional optical microscope. The main difference between TEM and SEM is that, in TEM, an image is formed from the interaction of the electrons transmitted through the specimen, whereas SEM detects the scattered/reflected electrons from the specimen surface.

Information can be obtained on morphology, topography, composition, and chemistry of the sample using a range of optional microanalysis techniques such as high-resolution TEM (HRTEM – to obtain images with atomic resolution), selected-area electron diffraction (SAED – to provide crystallographic information), energy-dispersive X-ray spectroscopy and electron-energy loss spectroscopy (EDX and EELS – to determine the elemental composition) and scanning transmission electron microscopy (STEM – bright field and dark field contrast imaging).

In this study, conventional imaging, HRTEM, STEM, SAED, and EDX modes of operation were applied for the characterization of samples. FEI Tecnai G2 F30 TEM (Figure 3.16) at an operating voltage of 300 kV was used for the imaging of Ga_2O_3 thin films and hafnia nanostructured samples. TEM specimens of Ga_2O_3 films were prepared by FEI Nova 600i Nanolab focused ion beam system, whereas HfO_2 nanofibers were imaged directly after a sonication and syringe-dispense process onto TEM Cu sample-grid.

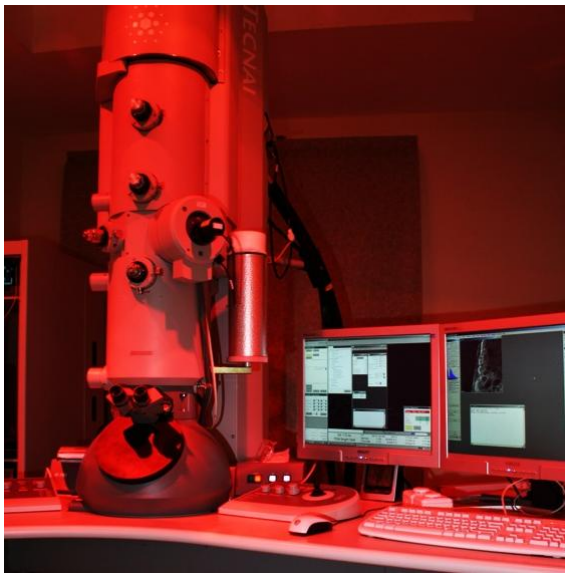

Figure 3.16: FEI Tecnai G2 F30 transmission electron microscope.

3.5.6 Spectroscopic Ellipsometry

Ellipsometry measures the change in polarization state of light upon reflection from a surface and is used for the optical and morphological characterization of surfaces, interfaces and thin films. An ellipsometric measurement includes the analysis of polarization change between the incident light, which is a collimated beam of monochromatic light with a known polarization state, and the reflected light. From the measured difference, various properties of the reflecting surface can be extracted, such as optical constants (refractive index and extinction coefficient), surface roughness, layer thickness, composition, and optical anisotropy.

In this study, spectroscopic ellipsometry (SE) was used for determining the thicknesses and optical constants of the films deposited via ALD. The instrument used is a Variable Angle Spectroscopic Ellipsometer (VASE©) made by J.A. Woollam Co. (Figure 3.17). Ellipsometric spectra of the Ga_2O_3 and In_2O_3 thin film samples were measured at three angles of incidence (65°, 70°,

and 75°) within the wavelength range of 300 - 1000 nm. Cauchy dispersion function was used for modeling the optical constants and estimating film thicknesses. Prior to depositions, native oxide thicknesses of the Si (111) substrates were measured by spectroscopic ellipsometry, which were then used for estimating the thicknesses of deposited Ga_2O_3 and In_2O_3 layers using the $Si/SiO_2/Ga_2O_3$ (In_2O_3) model. For samples without a native oxide layer, Si/material models were used.

Figure 3.17: J. A. Woolam V-VASE spectroscopic ellipsometer.

3.5.7 Ultraviolet-Visible Spectrophotometry

Ultraviolet-visible (UV-VIS) spectrophotometry is used to determine the absorption or transmission spectra in the UV-VIS spectral region. This means that it uses light in the visible and adjacent (near-UV and near-infrared (NIR)) ranges. Light absorption of UV and VIS light occurs due to absorption of incident photon energy by electrons which can be excited (such as π-electrons). With the help of Beer-Lambert law, the intensity of absorption of UV-VIS radiation can be correlated to the amount of substance presence in a sample.

Varian Cary 5000 UV-VIS-NIR spectrophotometer (Figure 3.18) was used to measure the absorbance of the as-deposited and annealed Ga_2O_3 films. Films

were deposited on double-side-polished sapphire substrates. Absorbance vs. wavelength graphs were obtained in the wavelength range of 200-800 nm.

Figure 3.18: Varian Cary 5000 UV-VIS-NIR Spectrophotometer.

3.5.8 Semiconductor Parameter Analyzer and DC-Probe Station

Semiconductor parameter analyzer was used for the measurement of electrical characteristics of the MOS capacitors. Capacitance of the dielectric Ga_2O_3 layer and the current passing through the device were analyzed by sweeping the voltage applied to the fabricated MOS capacitors. A probe station was used to physically acquire signals from the device by precise positioning of micro-needles on the surface of the semiconductor device. Keithley 4200-SCS semiconductor parameter analyzer and Cascade Microtech PM-5 DC probe station were used to obtain current-voltage and capacitance-voltage characteristics of Ga_2O_3 films (Figure 3.19).

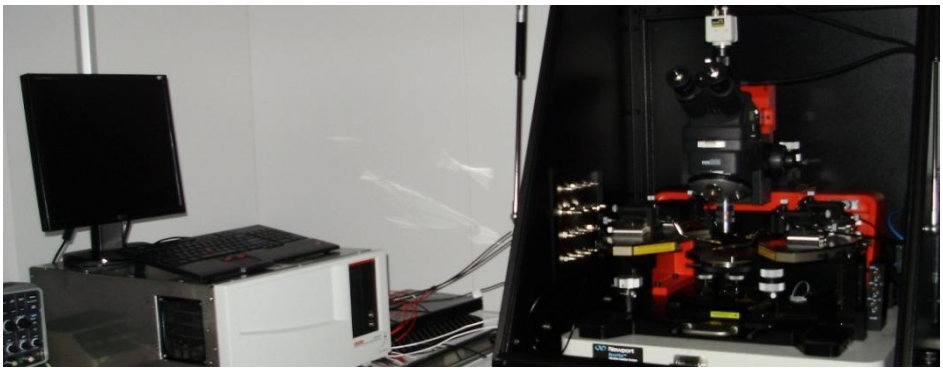

Figure 3.19: (Left) Keithley 4200-SCS semiconductor parameter analyzer, and (right) Cascade Microtech PM-5 DC-probe station.

Chapter 4

Results and Discussion

Recent ALD studies have often dealt with the growth mechanism investigations, but structural, optical and electrical properties of the grown films have been of interest as well. This chapter presents the experimental results of recipe optimization studies for Ga_2O_3 deposition along with the structural, optical and electrical properties of the deposited films. Additionally, efforts on optimization for ALD growth of In_2O_3 thin films are discussed. Results regarding to the template-based synthesis of HfO_2 nanotubes by combining electrospinning and ALD processes, and characterization of the resulting nanostructures are also included in this chapter.

4.1 PEALD of Ga_2O_3

4.1.1 Optimization of Deposition Parameters

Initially, TMG and high performance liquid chromatography grade H_2O process was tried for the deposition of Ga_2O_3 thin films using Svannah S100 thermal ALD system. However, this trial was unsuccessful, since TMG did not react with water and no film growth was observed from XPS and SE measurements.

Therefore, PEALD of Ga_2O_3 thin films was realized by the Fiji F200 LL PEALD system using O_2 plasma as the oxidant. Deposited films were confirmed to be Ga_2O_3 and the growth parameters were optimized accordingly.

In order to optimize growth parameters needed for the self-limiting deposition of Ga_2O_3 thin films, the effect of TMG dose, O_2 plasma duration, and Ar purge time were investigated. The effect of TMG pulse duration in the PEALD cycle was examined by performing a series of depositions, where TMG pulse time was changed while other parameters were kept constant. Doubling the TMG dose from 0.015 to 0.03 s (precursor bottle temperature ~6 °C) did not affect the deposition rate remarkably, indicating that 0.015 s is already high enough for TMG surface saturation. Figure 4.1(a) shows the deposition rate of Ga_2O_3 films as a function of O_2 flow duration. As can be seen from this graph, experiments were carried out using various durations ranging from 2 to 60 s. Deposition rate has saturated for O_2 flow durations starting from 10 s. Although 10 s was an acceptable value, 20 s was used for the following Ga_2O_3 recipe development experiments. The effect of purge time on the growth rate was also investigated. Purge durations of 5 and 10 s were resulted with the same deposition rate. In other words, 5 s of Ar flow was found to be sufficient for the complete purging of excess precursors and gaseous byproducts from the sample surface and reactor volume.

To study the effect of temperature on growth rate and determine the range of ALD window, 150 cycles with 0.015 s TMG and 20 s O_2 plasma were deposited at different temperatures (28-400 °C). A wide ALD temperature window was observed from 100 to 400 °C (Fig. 4.1 (b)), where the deposition rate was constant at ~0.53 Å/cycle. In Figure 4.1(c), Ga_2O_3 film thickness was plotted as a function of the number of PEALD cycles. Films deposited at 250 °C exhibited a linear growth behavior, and slope of the linear fit corresponded to the deposition rate observed within the ALD window.

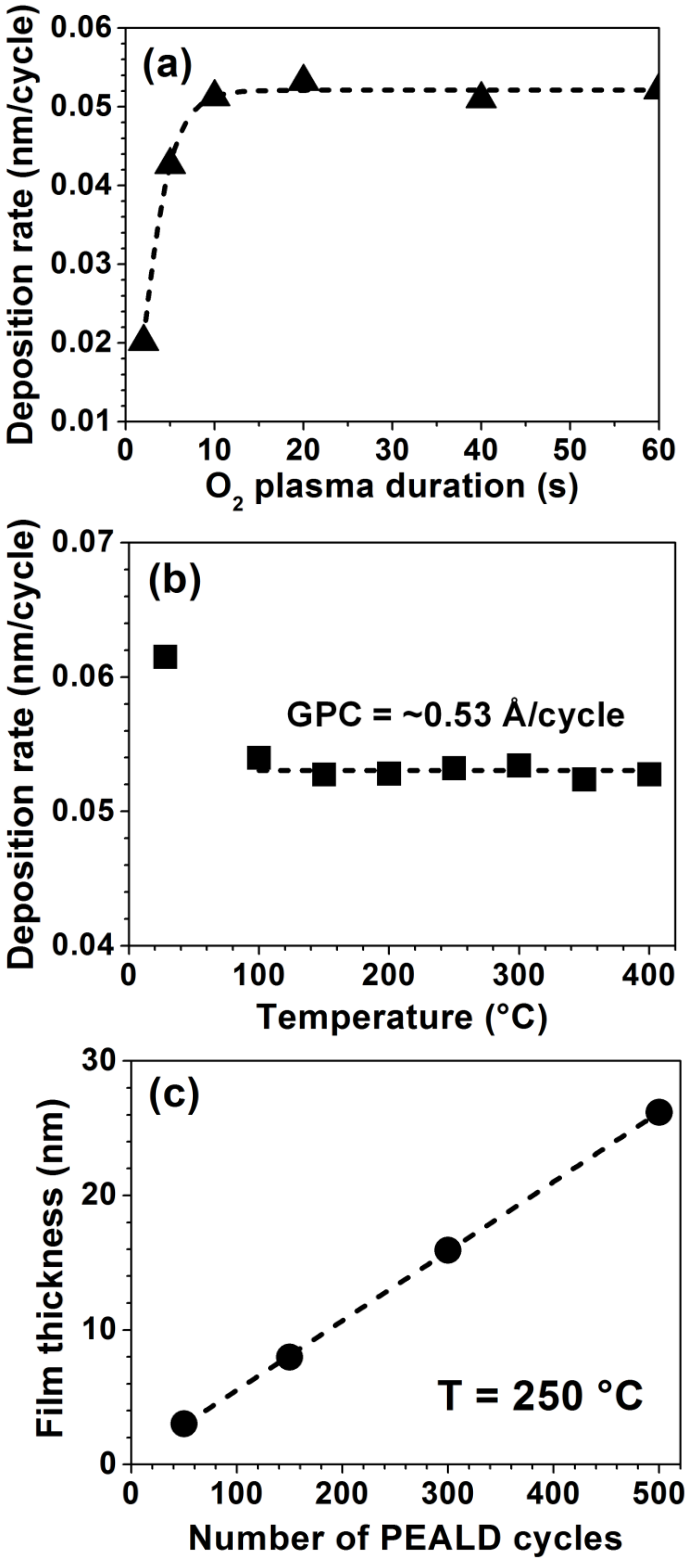

Figure 4.1: Growth rate of Ga_2O_3 thin films as a function of (a) O_2 plasma flow duration at 250 °C, and (b) deposition temperature. TMG dose and O_2 plasma flow rate were constant at 0.015 s and 25 sccm, respectively. (c) Ga_2O_3 film thickness as a function of the number of PEALD cycles.

4.1.2 Characterization of Ga_2O_3 thin films

4.1.2.1 Morphological Characterization

As-deposited Ga_2O_3 thin films were observed to be continuous and smooth from the SEM micrographs. However, after a post-growth annealing treatment at 900 °C under N_2 atmosphere, surface became discontinuous, with nano-scale cracks formed on the samples. These cracks were few hundreds of nanometers in length and homogeneously distributed along the whole sample (Figure 4.2(b)). The reason of crack formation upon annealing may be related to the thermal expansion coefficient (CTE) mismatch between the Ga_2O_3 film and Si substrate. CTE of Ga_2O_3 was reported between 8.2 and 8.5 ppm/°C [69], whereas CTE of Si is 2.6 ppm/°C.

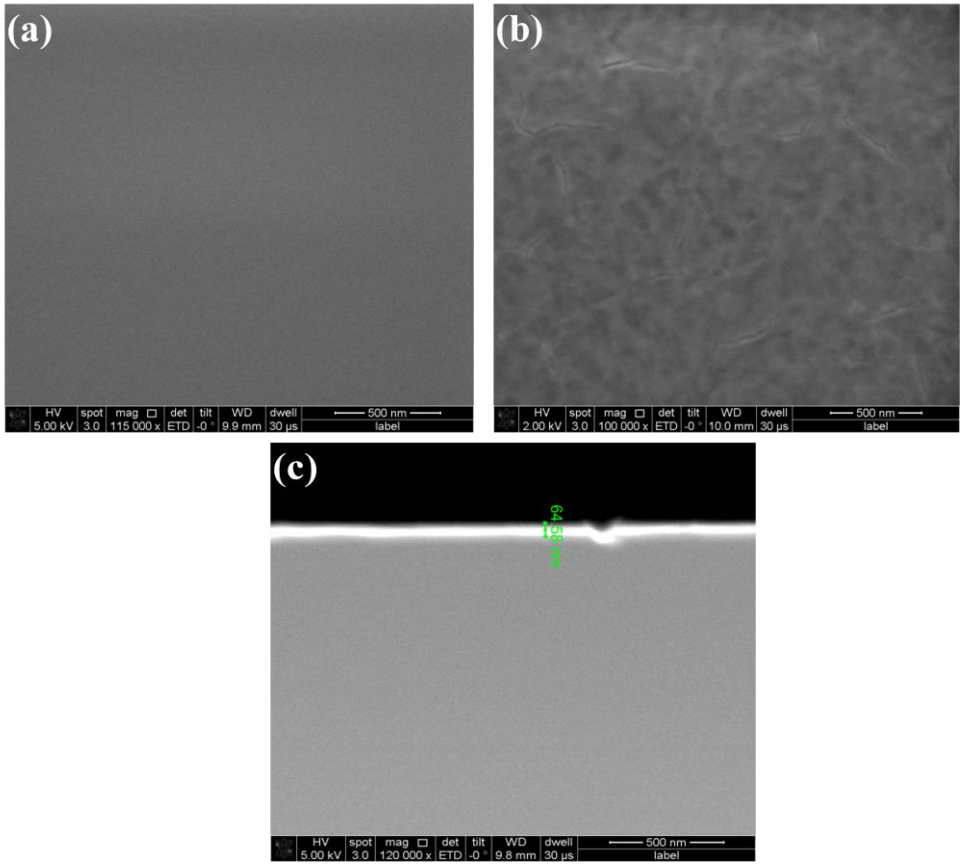

Figure 4.2: Plan-view SEM images of (a) as-deposited and (b) annealed Ga_2O_3 thin films (c) Cross-sectional SEM image of the as-deposited thin film. For all images, Ga_2O_3 thin film was deposited using 1200 PEALD cycles.

Besides crack formation, flake-like structures were observed at the surface of annealed films (Figure 4.3). These structures were not observed for the annealed films deposited with 120 and 500 cycles. For the films deposited using 800 and 1200 cycles, on the other hand, surface-density of flake-like structures increased with increasing number of deposition cycles. Shape of these structures were almost the same for all annealed samples; however, they became bigger and more evident with increasing annealing temperature. In literature, formation of the similar structures upon crystallization after annealing was reported for various thin films including CuO/SiO_2, MoS_2, and $Ni_{0.8}Zn_{0.2}Fe_2O_4$ [70-72].

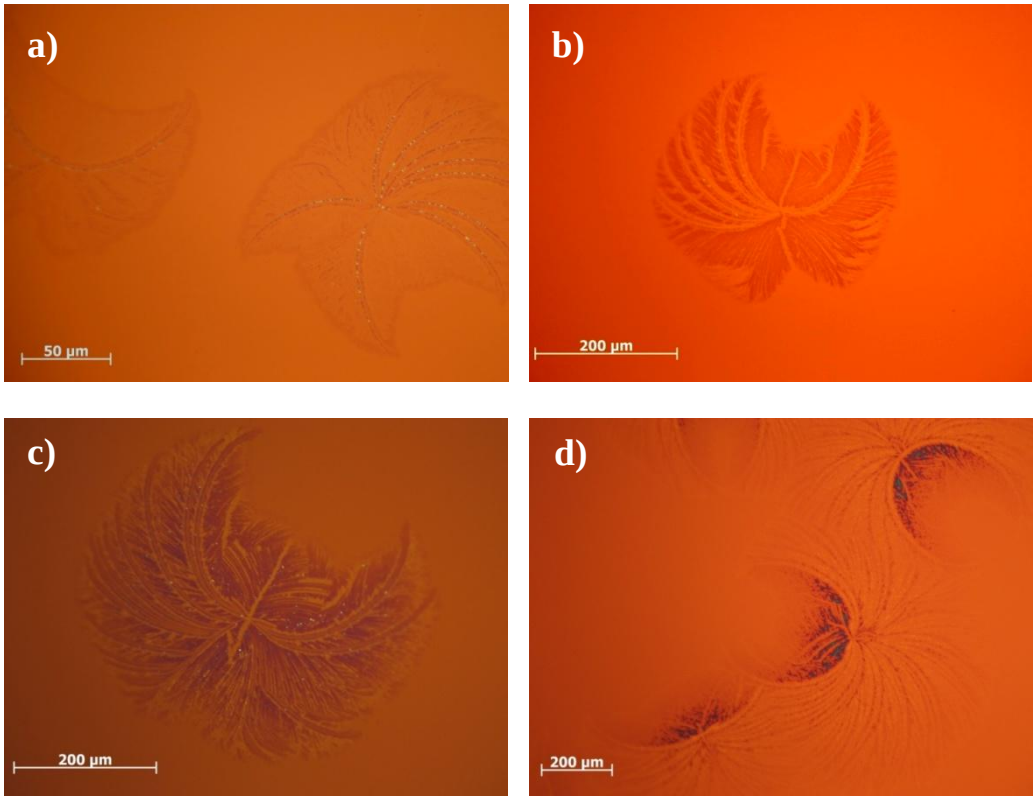

Figure 4.3: Optical microscope images of ~65-nm-thick Ga_2O_3 thin films annealed under N_2 atmosphere for 30 minutes at (a) 700 °C, (b) 800 °C, (c) 900 °C, and (d) 1000 °C.

To further study the morphology of Ga_2O_3 films, AFM analyses were performed. Change in the rms roughness values with respect to film thickness and annealing temperature was investigated. Figure 4.4 shows the 3D AFM

topographies of as-deposited and annealed samples deposited by 500 PEALD cycles, corresponding to ~26 nm film thickness. Rms roughness value, which was measured from a 1 μm x 1 μm scan area, increased from 0.16 to 0.37 nm after annealing at 900 °C for 30 min. This increase in the rms roughness value was attributed to the formation of grains upon crystallization and crack formation, which was also observed from SEM micrographs.

In addition to annealing temperature, the effect of film thickness on roughness was also investigated. For this purpose, as-deposited Ga_2O_3 films deposited with different number of cycles were characterized using AFM. Roughness values of the films increased with increasing thickness. In Table 4.1, roughnesses of Ga_2O_3 thin films for different number of PEALD cycles are listed.

Table 4.1: Rms roughness values of the as-deposited Ga_2O_3 thin films.

Number of PEALD cycles	**Film thickness (nm)**	**Rms roughness (nm)**
500	26.2	0.161
800	45.5	0.218
1200	67.2	0,.291

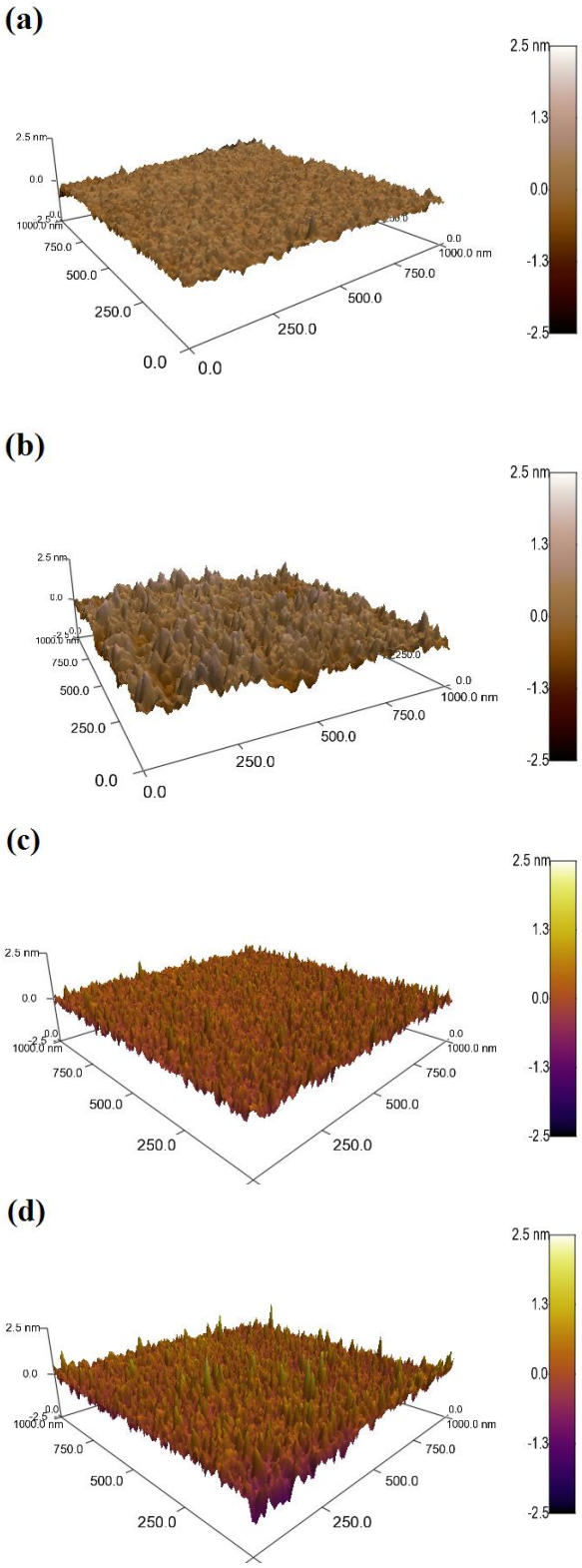

Figure 4.4: AFM images of (a) as-deposited, and (b) annealed Ga_2O_3 thin films grown using 500 PEALD cycles. As-deposited Ga_2O_3 thin films deposited using (c) 800, and (d) 1200 PEALD cycles.

4.1.2.2 Elemental Characterization

Chemical compositions and bonding states of the deposited Ga_2O_3 thin films were studied by XPS. Survey scans detected peaks of gallium (Ga), oxygen (O), and carbon (C) with the concentrations of ~33.6, ~51.4, and ~15.0, at.%, respectively, for the film deposited at 250 °C. Almost same elemental compositions were measured for the films deposited at different temperatures within the ALD window. The reason of C found in the samples was asserted to be due to surface contamination. In order to prove this claim, films were etched for 60 s by applying ion beam etching with 2 kV Ar ions; C was not detected in the bulk film.

Ga 3d high resolution XPS spectrum taken from the surface of a ~26 nm-thick Ga_2O_3 sample was fitted using two subpeaks as shown in Figure 4.5 (a). Subpeak #1, with a binding energy of 21.2 eV, confirmed the presence of Ga-O bond in the samples. Subpeak #2 (~25 eV), on the other hand, was related to the contribution from O 2s core level [73]. The effect of this contribution on XPS survey scan results is also noteworthy, which leads to an overestimation of the Ga atomic concentration in deposited films. Figure 4.5(b) is the O 1s high resolution XPS spectrum taken from the sample surface. Binding energy position of the O 1s (532.3 eV) core level was well consistent with the literature [74].

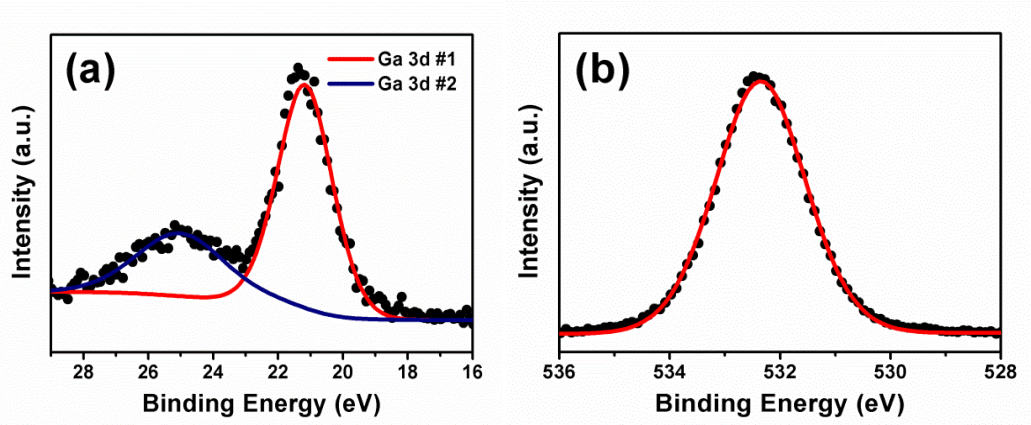

Figure 4.5: (a) Ga 3d, and (b) O 1s high resolution XPS scans of ~26-nm-thick Ga_2O_3 thin film deposited at 250 °C.

In order to study the uniformity of elemental composition towards the bulk film and interface, depth profile analyses were performed on a ~26 nm-thick films. In Figures 4.6(a) and (b), depth profiles of the as-deposited and annealed films are shown, respectively. Measurements were recorded for each film using the exact same sputtering procedure. C was detected only at the film surface and was completely removed after 10 s of ion etching, indicating that it originates from surface contamination. Uniform composition throughout the bulk film was observed for all samples.

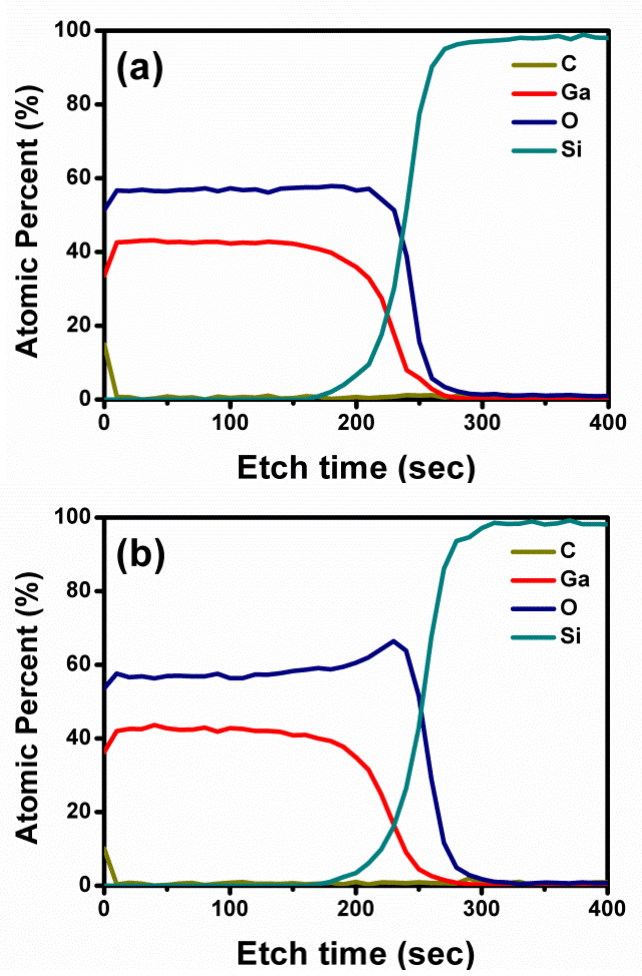

Figure 4.6: (a) Depth profile analysis results of the ~26 nm thick film deposited at 250 °C (b) Depth profile of the same sample after annealing at 900 °C.

Atomic concentrations of elements at the surface and in bulk film after 100 s of ion etching are listed in Table 4.2. Highest Ga/O ratios were found for

the annealed samples. O content was observed to increase at the interface, featuring the oxide formation at the Ga_2O_3-Si interface. This claim was also confirmed by TEM images, which will be presented in following section.

Table 4.2: Atomic concentrations of Ga, O, and C elements in the as-deposited and annealed thin films. Annealing process was applied at 900 °C under N_2 atmosphere for 30 min.

	As-deposited		**Annealed**	
	Film surface	Bulk film	Film surface	Bulk film
Ga (at.%)	33.64	41.3	36.3	43.61
O (at.%)	51.42	58.7	53.6	56.39
C (at.%)	14.94	0	10.1	0
Ga/O	**0.654**	**0.704**	**0.677**	**0.773**

4.1.2.3 Structural Characterization

Figure 4.7 shows the GIXRD patterns of as-deposited and annealed Ga_2O_3 films. Although these patterns belong to a film deposited at 250 °C, PEALD-grown Ga_2O_3 thin films were found to be nanocrystalline in the as-deposited state irrespective of their deposition temperature.

Upon annealing at 900 °C for 30 min under N_2 atmosphere, polycrystalline β-Ga_2O_3 films with a monoclinic crystal structure were obtained (ICDD reference code: 00-011-0370). Among all the five different allotropic modifications of Ga_2O_3, β-Ga_2O_3 is known to be the most stable and frequent one reported for thin films [75]. In order to determine the annealing temperature at which crystallization starts, as-deposited samples were annealed at 500, 600, 700, and 800 °C for 30 min under N_2 atmosphere. GIXRD patterns of these samples indicated that crystallization starts at 600 °C. Crystallinity of the β -Ga_2O_3 films increased with annealing temperature.

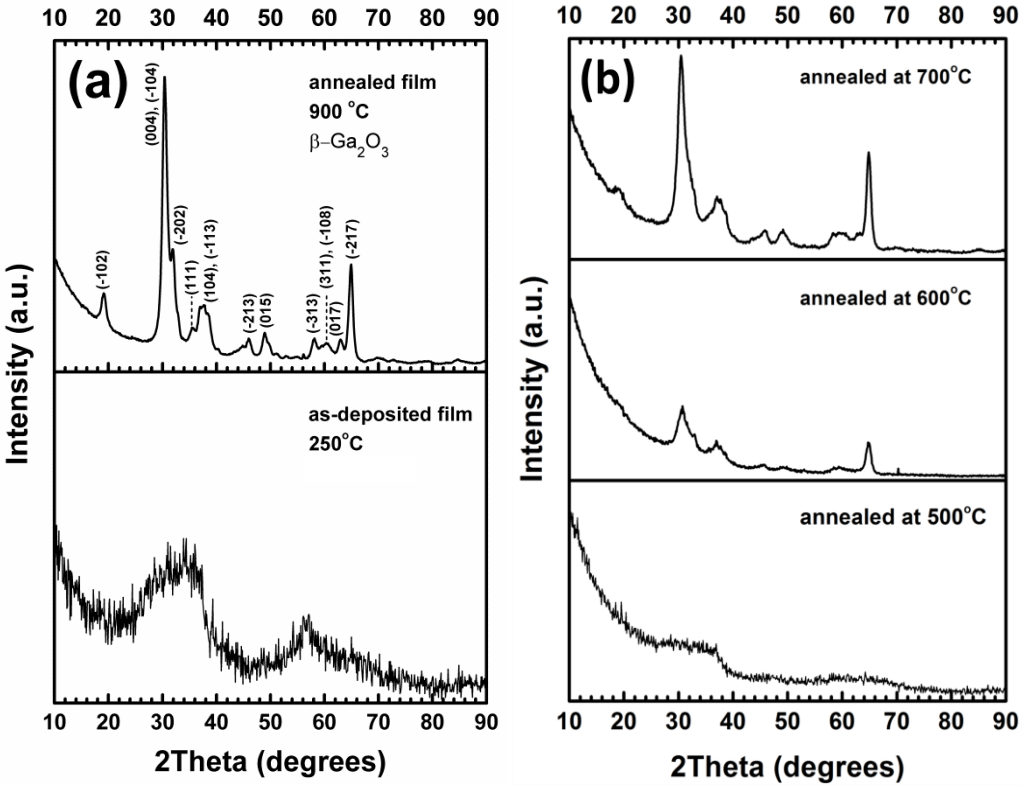

Figure 4.7: (a) GIXRD patterns of a ~26 nm-thick Ga_2O_3 thin film. Film deposited at 250 °C was amorphous in the as-deposited state. GIXRD pattern of the annealed film ($T_{annealing}$ = 900 °C) revealed a polycrystalline structure that corresponds to the β-Ga_2O_3 phase. (b) GIXRD patterns of Ga_2O_3 thin film samples annealed at 500, 600, and 700 °C.

Figure 4.8(a) is the HRTEM image of the Ga_2O_3 film deposited on Si (111) at 250 °C. Film thickness was measured as 26.7 nm from this image, which is in good agreement with the results obtained by ellipsometry. From this image, nanocrystalline nature of the as-deposited film is also seen. Moreover, Si-Ga_2O_3 interface is not as smooth as expected, which is probably due to the TEM sample preparation procedure applied. The nanocrsytalline structure of the as-deposited film was further confirmed by SAED measurements (Figure 4.8(b)).

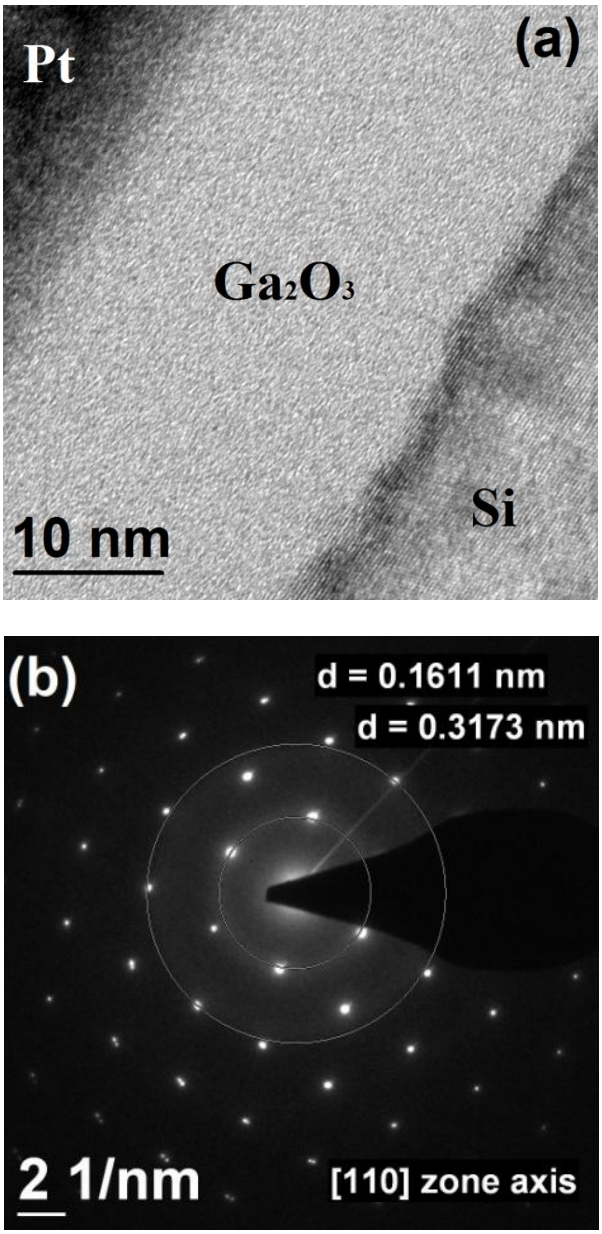

Figure 4.8: (a) Cross-sectional HRTEM image of the Ga_2O_3 thin film deposited on Si (111) at 250 °C. (b) SAED pattern of the same sample.

As can be seen from Figure 4.9 (a), after annealing at 900 °C under N_2 ambient, ~7 nm-thick SiO_2 layer was formed at the Si-Ga_2O_3 interface. This behavior was also observed from XPS measurements. SiO_2 formation at the metal-oxide-Si interface was previously reported in several studies [27]. It is known that oxide formation at the interface is due to the ease of oxidation of Si substrate [76]. Besides the SiO_2 formation, Ga_2O_3 film became polycrystalline

upon annealing as can be seen from Figure 4.9(b). Crystal structure of the annealed sample was determined as monoclinic (i.e. β-Ga_2O_3), by the GIXRD measurements. From the inset of Figure 4.9 (b), polycrystalline diffraction rings can be observed.

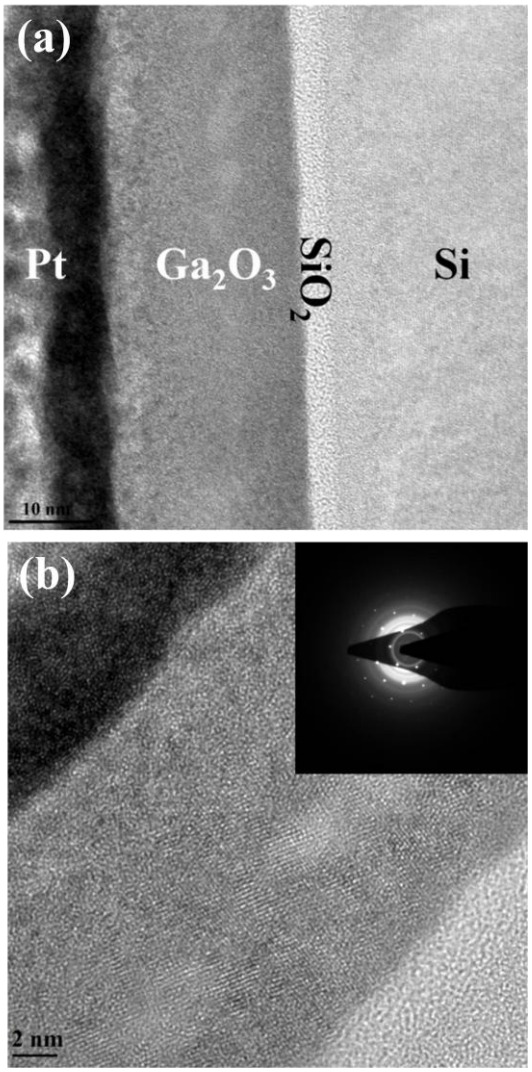

Figure 4.9: (a) Cross-sectional TEM image of the Ga_2O_3 thin film after post-growth annealing at 900 °C under N_2 ambient. (b) HRTEM image of the same sample. Inset shows the SAED pattern consisting of polycrystalline rings.

4.1.2.4 Optical Characterization

Thicknesses and optical constants of Ga_2O_3 thin films were estimated by modeling the spectra measured by spectroscopic ellipsometry within the wavelength range of 300-1000 nm. Ellipsometric spectra of the as-deposited and annealed Ga_2O_3 thin films (500 PEALD cycles) were modeled by the Cauchy dispersion function using Si (0.5 mm)/SiO_2/Ga_2O_3 layer structure. Thickness of the as-deposited film was measured as 26.2 nm, which did not change remarkably after the post-growth annealing. Refractive index values, on the other hand, increased from 2.05-1.86 to 2.09-1.92 within the 300-1000 nm spectral range (Figure 4.10). These results again indicate structural enhancement and film densification upon annealing at 900 °C.

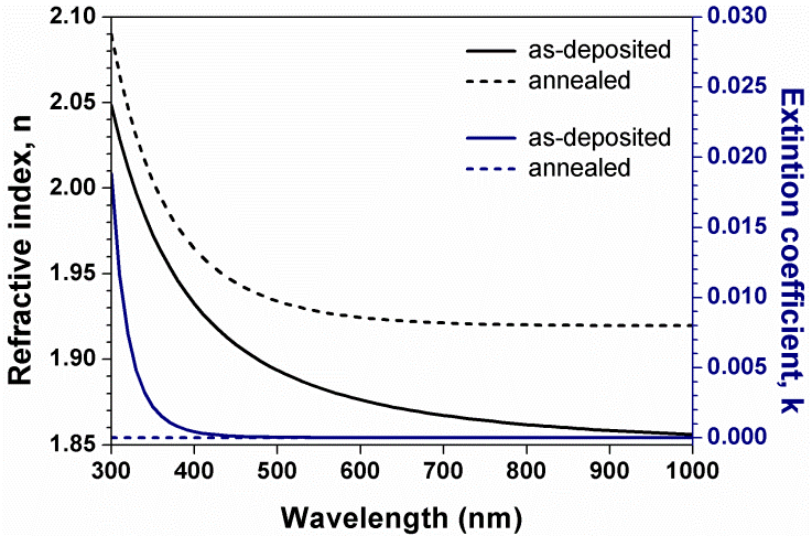

Figure 4.10: Refractive indices and extinction coefficients of the as-deposited (250 °C) and annealed ~26 nm thick Ga_2O_3 thin films.

From the UV-VIS spectra, absorbance vs. wavelength graphs were obtained for as-deposited and annealed 45.5 nm-thick Ga_2O_3 films. Band gap energies were estimated by assuming a direct transition between the conduction and valence bands. The optical band gaps (E_g) of as-deposited and annealed films were evaluated from the plot of α^2vs. photon energy (hv) and shown in

Figure 4.11. The E_g values were found by extrapolation of the linear portion of the curve to the energy axis at $\alpha^2 = 0$. E_g values of as-deposited and annealed Ga_2O_3 films were found as 5.10 and 5.14 eV, respectively.

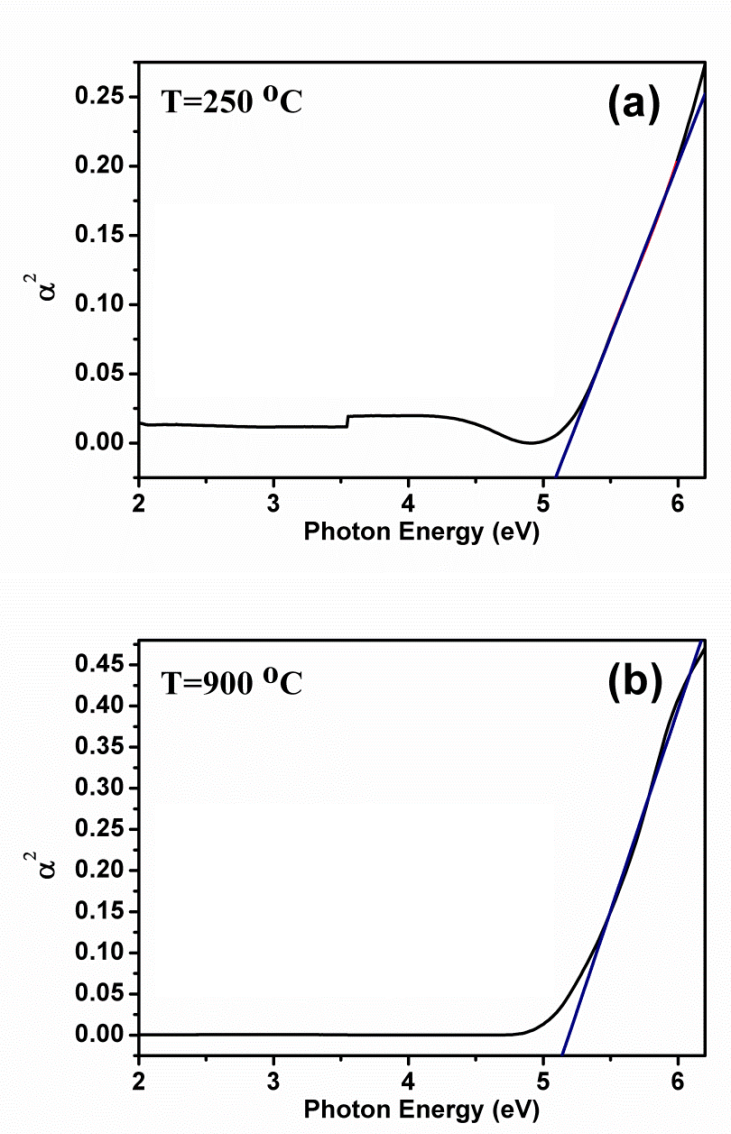

Figure 4.11: α^2 vs. photon energy spectrum for (a) as-deposited and (b) annealed 45.5-nm-thick Ga_2O_3 films.

4.1.2.5 Electrical Characterization

Following the fabrication of MOS capacitor structures, devices were electrically characterized in the form of standard capacitor structures. The standard capacitor characterization consists of capacitance voltage (C-V) and current voltage (I-V) measurements. As-deposited samples grown at 250 °C did not exhibit any prominent dielectric characteristic, thus all measurements belong to annealed samples. In this section, thickness and the annealing temperature dependence of electrical characteristics will be presented.

C-V characteristics of the 7.5 nm-thick films were measured by sweeping the voltage to positive and negative values (Figure 4.12). For the films annealed at 700 °C, C-V curves collapsed for voltages higher than 2V, which is attributed to the leakage from the top contact. While a large positive shift was observed for the film annealed at 700 °C, flat-band voltages were found to be positioned at zero after annealing at 900 °C. These C-V curves indicate high-quality interface with Si substrate and perfect dielectric characteristics. In addition, it has been shown that even a 7.5 nm-thick film can withstand high voltages (i.e. from -12 V to 12 V). Hysteresis window was also observed to be narrower for the film annealed at higher temperature.

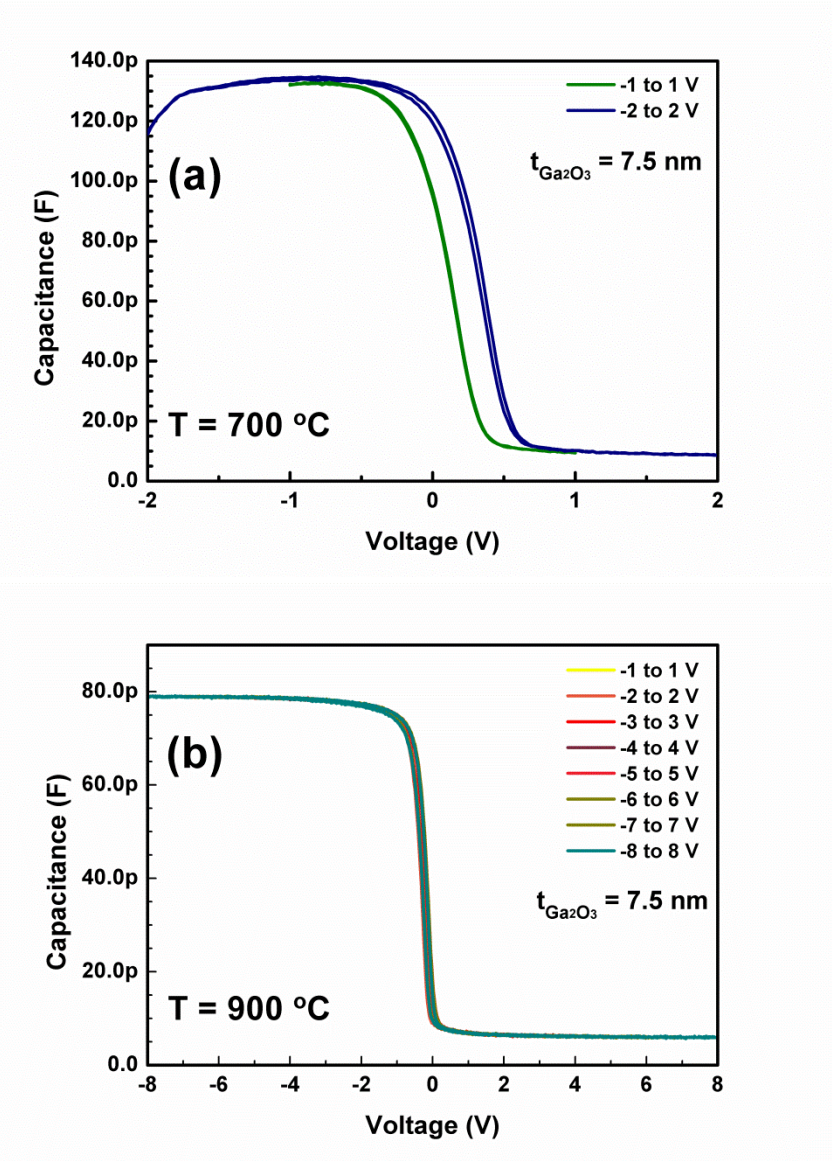

Figure 4.12: Capacitance-voltage (C-V) characteristics of MOS capacitor fabricated with 7.5-nm-thick Ga_2O_3 films annealed at (a) 700 °C and (b) 900 °C.

Dielectric constant "ε_{ox} "of the Ga_2O_3 layer can be estimated from the simple parallel capacitor model (Figure 4.13), which can be written as follows:

$$C_{ox} = \frac{\varepsilon_{ox}\, \varepsilon_o\, A}{t_{ox}} \qquad (4.1)$$

where C_{ox} is the oxide capacitance, A is the overlapping surface area of the plates, ε_o is the permittivity of free space (8.854 x 10^{-12} F/m), ε_{ox} is the relative dielectric permittivity of Ga_2O_3 film, and t_{ox} is the thickness of the insulating Ga_2O_3 layer.

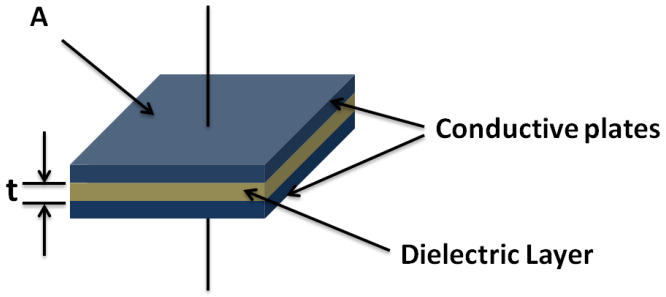

Figure 4.13: Parallel-plate capacitor model.

From Eqn. 4.1, dielectric constants of the films annealed at different temperatures were calculated and presented in Table 4.3 and Figure 4.14. Dielectric constants were observed to be slightly decreasing with increasing annealing temperature. The reason of this decrease may be related to the SiO_2 formation at the film-substrate interface, which was already evidenced by the TEM studies. XPS studies also confirmed the formation of an oxide layer at the interface. Similarly, oxide formation at the Ga_2O_3-Si interface was also reported in the literature [27]. SiO_2 was known to have a dielectric constant of ~3.9 [77]. Therefore, when this oxide layer increased in thickness with annealing at higher temperatures, the effective dielectric constant of the overall structure decreased.

Table 4.3: Dielectric constants of Ga_2O_3 films with respect to film parameters and annealing temperatures.

Film parameters		**Dielectric constants as a function of annealing temperature**		
Number of ALD cycles	**Thickness (nm)**	**700 °C**	**800 °C**	**900 °C**
120	7.5	3.766	3.391	3.013
400	22.5	8.361	7.005	6.891
800	45.5	10.282	9.139	8.852
1200	67.2	10.124	9.786	9.449

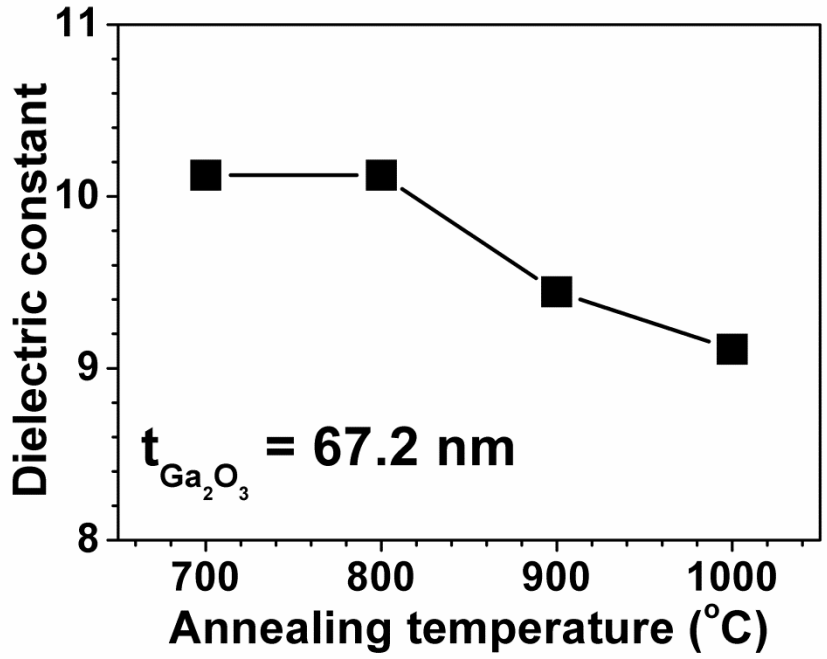

Figure 4.14: Dielectric constant of a 67.2 nm-thick annealed Ga_2O_3 thin film as a function of annealing temperature. Lines are for visual aid.

In Figure 4.15, thickness dependence of the dielectric constant is shown. Dielectric constant was observed to be increasing with increasing Ga_2O_3 film thickness. It is widely known that the film thickness of thin films has a strong effect on the dielectric constant, which is investigated in several studies [78, 79]. Thickness dependence of dielectric constant is due to presence of voids and discontinuities in the thin films. With the increase of film thickness, these voids and discontinuities are likely to be filled up and dielectric constant increases up to a constant value. At that value, films are thought to be free of voids etc. and dielectric constants of these thicker films will tend to be same as that of bulk material [80].

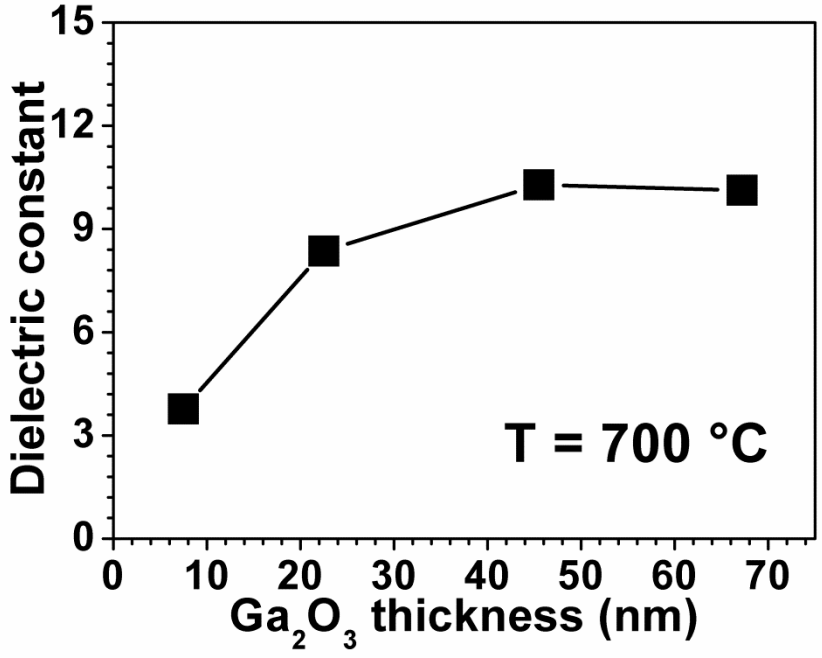

Figure 4.15: Dielectric constants of Ga_2O_3 thin films with respect to film thickness after annealing at 700 °C. Lines are for visual aid.

Figure 4.16(a) belongs to a MOS structure with a 67.2 nm-thick (1200 PEALD cycles) annealed ($T_{annealing}$ = 800 °C) Ga_2O_3 layer. As also evident from this image, a characteristic C-V curve could not be obtained for the structures with thick Ga_2O_3 layers (800 and 1200 PEALD cycles). This behavior is possibly due to the crack formation, which was observed for the thick Ga_2O_3 films and reported at the morphological characterization section. In order to prevent the effect of cracks, ~5 nm-thick Al_2O_3 film was coated onto Ga_2O_3 films subsequently after the annealing. Measurement results obtained from the resulting structure is given in Fig. 4.16(b). A large charge trapping hysteresis was observed with a positive shift of flat-band voltage when the applied gate voltage is increased. This positive shift in the flat-band voltage indicates the presence of negative charges in the oxide layer.

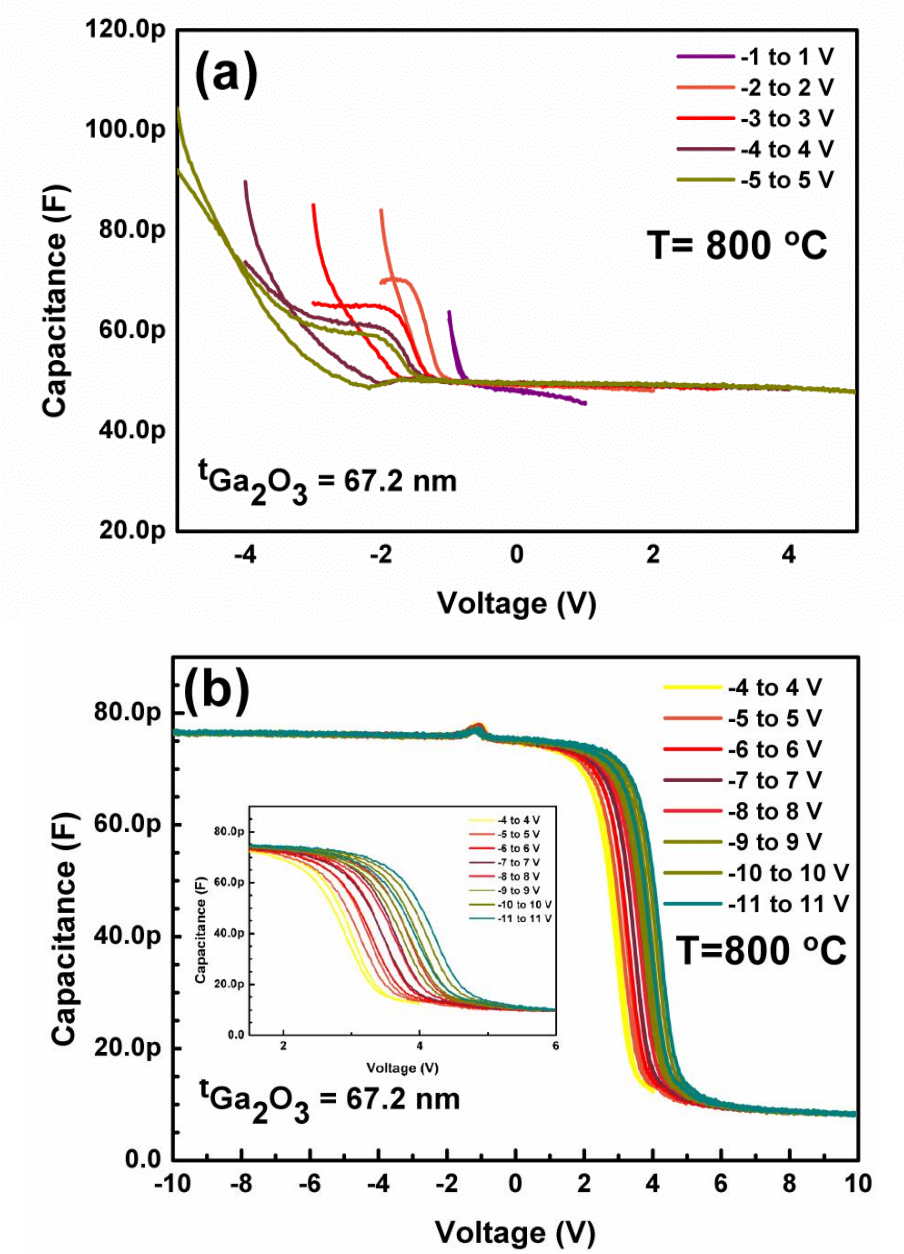

Figure 4.16: (a) C-V curves of MOS capacitors fabricated with a 67.2 nm-thick Ga_2O_3 films annealed at 800 °C. (b) C-V curves of the same sample, which were obtained after it was coated with a ~5 nm-thick Al_2O_3 layer.

C-V characteristic of the MOS capacitor with a 67.2-nm-thick Ga_2O_3 film annealed at 700 and 1000 °C is given in Figure 4.17. As seen from this figure, the hysteresis window gets broadened with higher annealing temperatures. It can be also stated that the charge trapping effect increases at higher annealing

temperatures. In addition, positive shift decreases with increasing annealing temperatures, which indicates the elimination of interface charges.

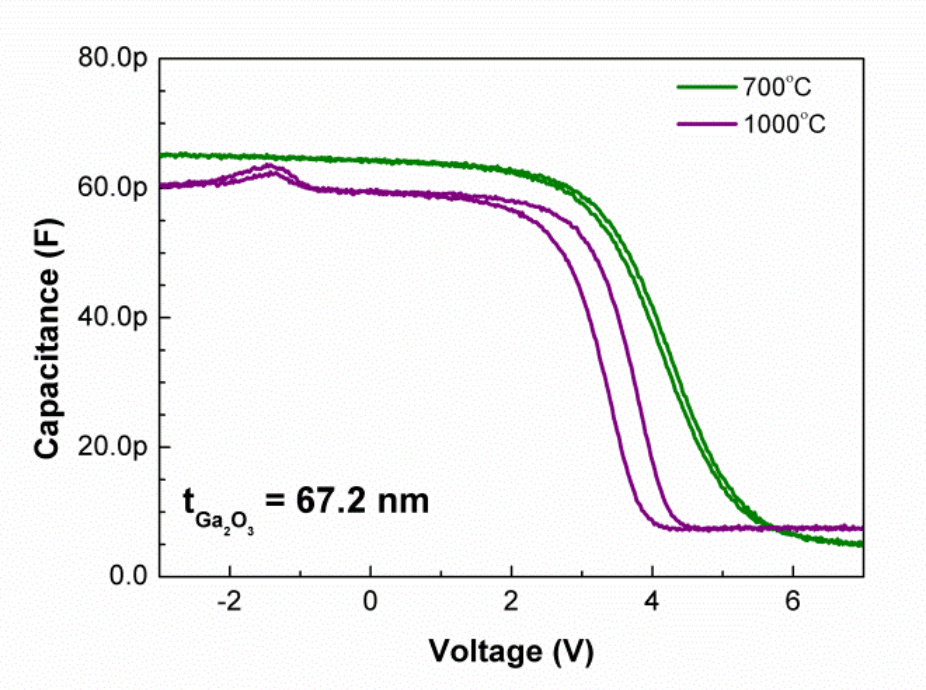

Figure 4.17: C-V curves of a MOS capacitor with 67.2-nm-thick insulating Ga_2O_3 layer, which was subjected to post-growth annealing at different temperatures.

Thickness dependence of the C-V characteristics was studied for all annealing temperatures. In Figure 4.18, C-V curves of the MOS devices consisting of Ga_2O_3 layers deposited using 120 (7.5 nm), 400 (22.5 nm) and 1200 (67.2 nm) PEALD cycles are given. With the increasing number of PEALD cycles, flat-band voltage shifted to positive values. Flat-band voltage was found to be about -0.2, 1.08, and 3.85 V for films deposited with 120, 400, and 1200 cycles, respectively. Oxide layer at the Ga_2O_3-Si interface is expected to be thicker for thicker Ga_2O_3 films. Therefore, more oxygen vacancies would be formed and trapped in the film. In addition, increase in Ga_2O_3 film thickness resulted in a wider hysteresis window.

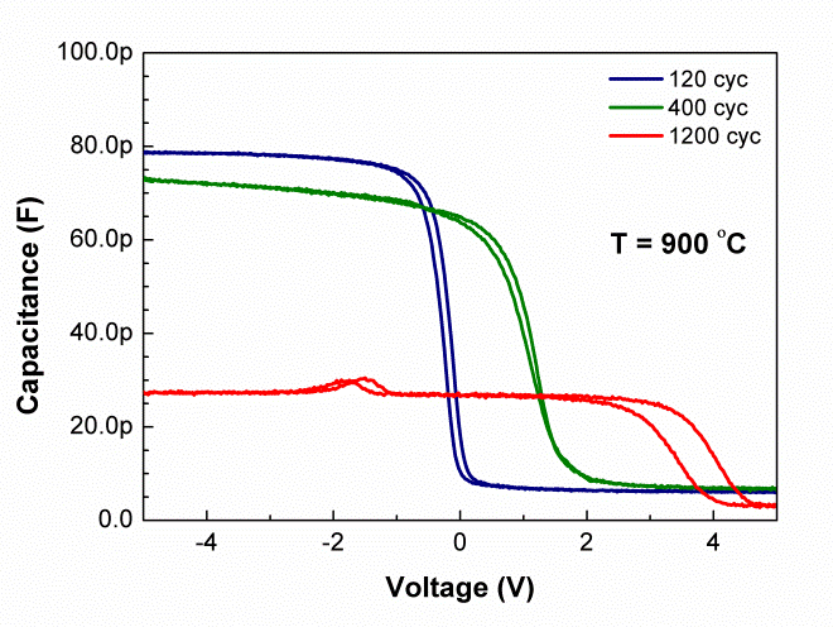

Figure 4.18: C-V measurement results of a MOS capacitor with Ga_2O_3 films annealed at 900 °C with respect to film thickness.

Figure 4.19 shows the I-V characteristics of 7.5 and 22.5 nm-thick Ga_2O_3 films annealed at various temperatures under positive bias. As can be seen from this figure, increasing the thickness results in a finite on-set voltage for the current to flow through the dielectric layer. Ga_2O_3 films annealed at higher temperatures resulted in a lower saturation current indicating the improved dielectric quality.

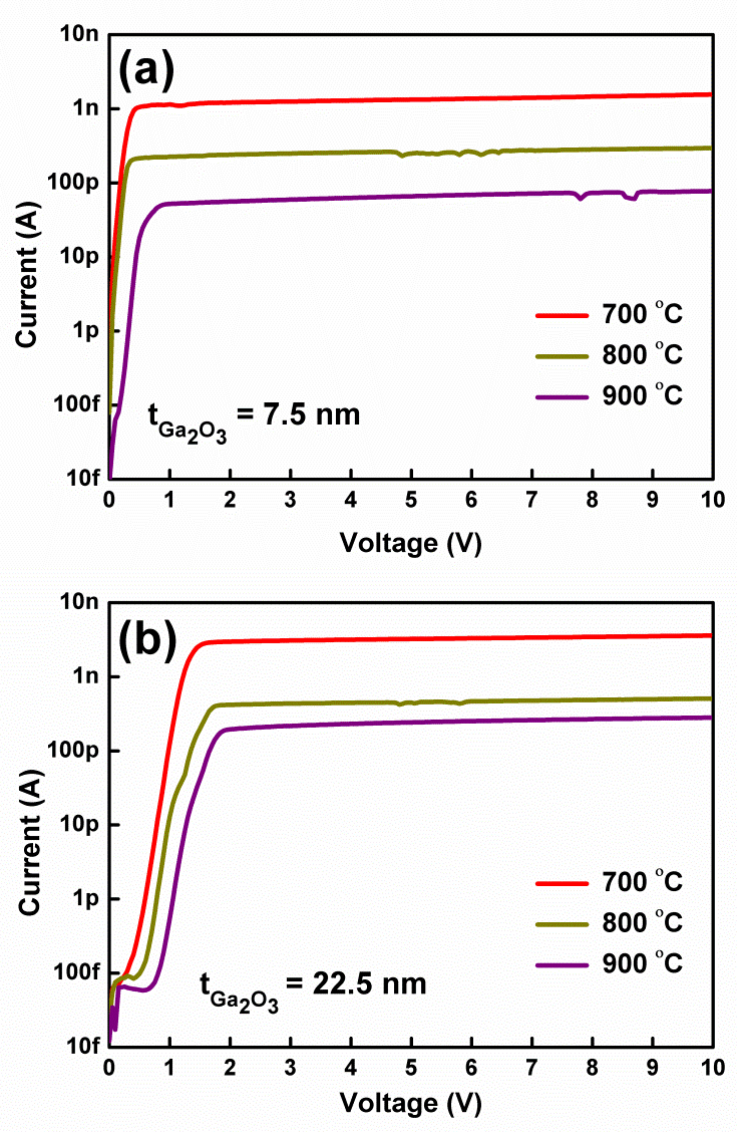

Figure 4.19: I-V characteristics of MOS capacitors with Ga_2O_3 thin films annealed at different temperatures.

From Figure 4.20, it can be stated that breakdown voltages of the MOS capacitors increased with annealing temperatures. Taking 10 μA current value as reference, breakdown voltages were measured as 28, 38, and 116 V for the structures with Ga_2O_3 thin films annealed at 700, 800 and 900 °C, respectively.

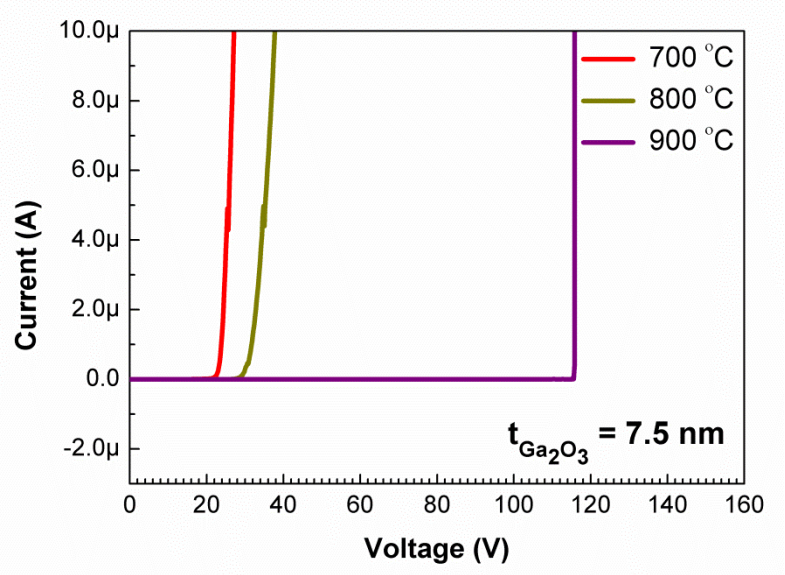

Figure 4.20:I-V characteristics of MOS capacitors fabricated with 7.5 nm-thick Ga_2O_3 thin films annealed at different temperatures.

4.2 PEALD of In_2O_3

First, saturation behavior of the cyclopentadienyl indium (CpIn) was studied while O_2 plasma duration and flow rate was set to 20 s and 25 sccm at 250 °C (Figure 4.21). However, no saturation was observed for CpIn pulse durations from 0.1 to 1.5 s. As a reason, it is thought that 250 °C might not be included in the ALD window and CpIn may be decomposing at this temperature. Therefore, CpIn saturation behavior was re-studied at 150 °C. This time, CpIn saturated for the pulse durations ranging from 0.2 to 1.8 s with a constant deposition rate of ~0.51 Å/cycle. One second was chosen as the optimum pulse duration to achieve saturation and used for the following growth optimization studies.

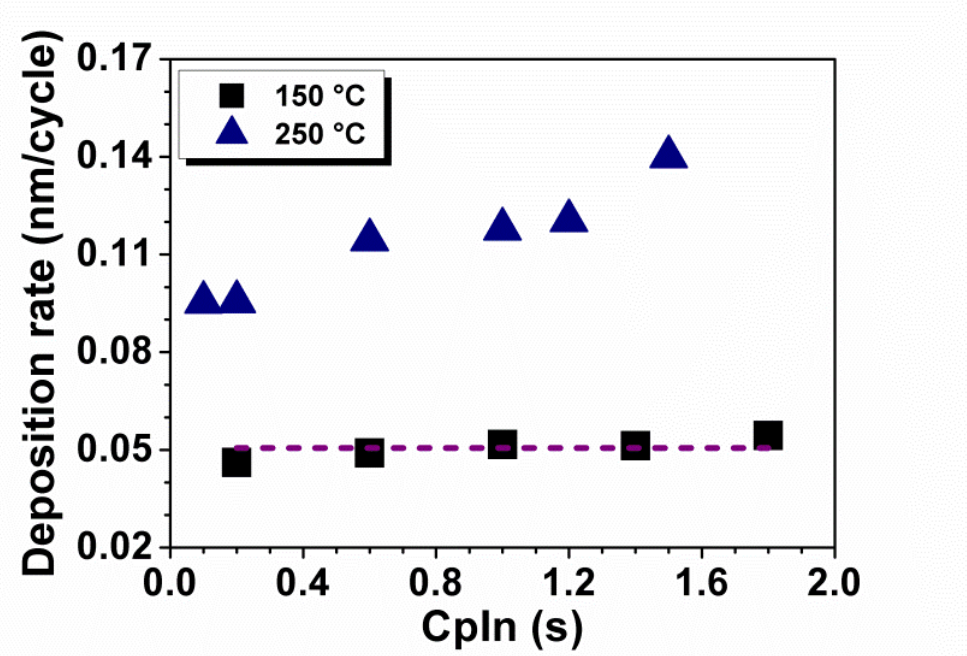

Figure 4.21: Saturation curves for cyclopentadienyl indium (CpIn) at 150 and 250 °C.

Then, the saturation behavior of O_2 plasma half-cycle was studied with 1 s CpIn pulses and different O_2 flow rates. For 25 sccm flow rate (Figure 4.22), saturation was not achieved until the plasma duration of 180 s. Therefore, 50 and 100 sccm O_2 flow rates were also studied and saturation has not yet been observed. From Table 4.4, it is observed that for a constant dose (flow rate x flow duration), deposition rate increased with flow duration. Optimization studies for the O_2 plasma saturation have not yet been completed. Thus, other growth parameters such as ALD window and effect of purge time have not yet been studied.

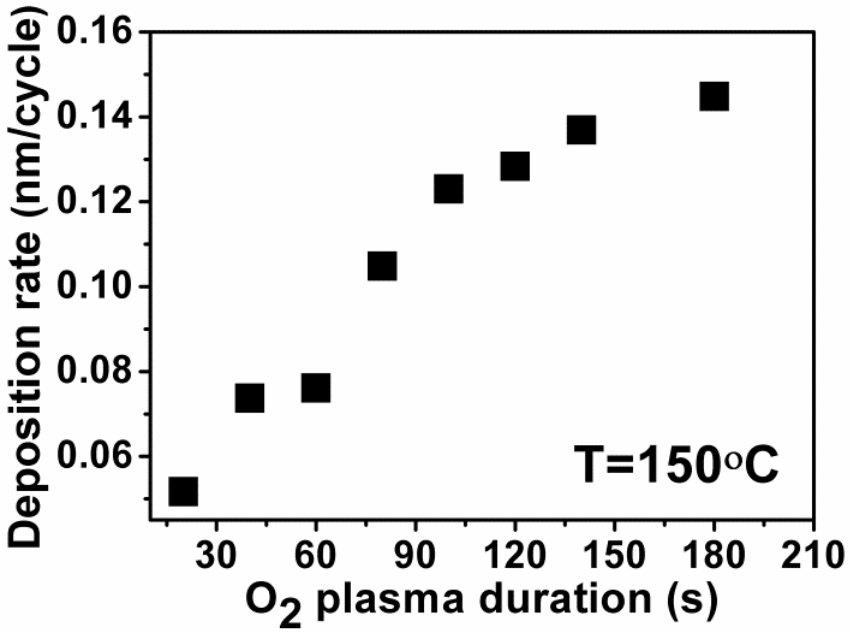

Figure 4.22: O_2 plasma duration vs. deposition rate at 150 °C.

Table 4.4: Deposition rate as a function of O_2 flow parameters.

O_2 flow rate	**O_2 flow duration**	**O_2 dose**	**Deposition rate**
sccm	**s**	**sccm * s**	**Å/cycle**
25	80	2000	1.05
50	40	2000	0.94
100	20	2000	0.75

In order to study the bonding states of deposited films, XPS high resolution scans were obtained. In 3d high resolution spectrum with peaks at the binding energies of 444.3 and 451.9 eV revealed the In-O bonding state (Figure 4.23(a)). O 1s spectrum was also fitted by two subpeaks, and the subpeak #1 at 529.6 eV was related to O-In bond. Thicknesses of the samples were lower than 10 nm; therefore, the subpeak at 531.5 eV was related to O-Si bond that exist in the native oxide layer at film-substrate interface (Figure 4.23(b)).

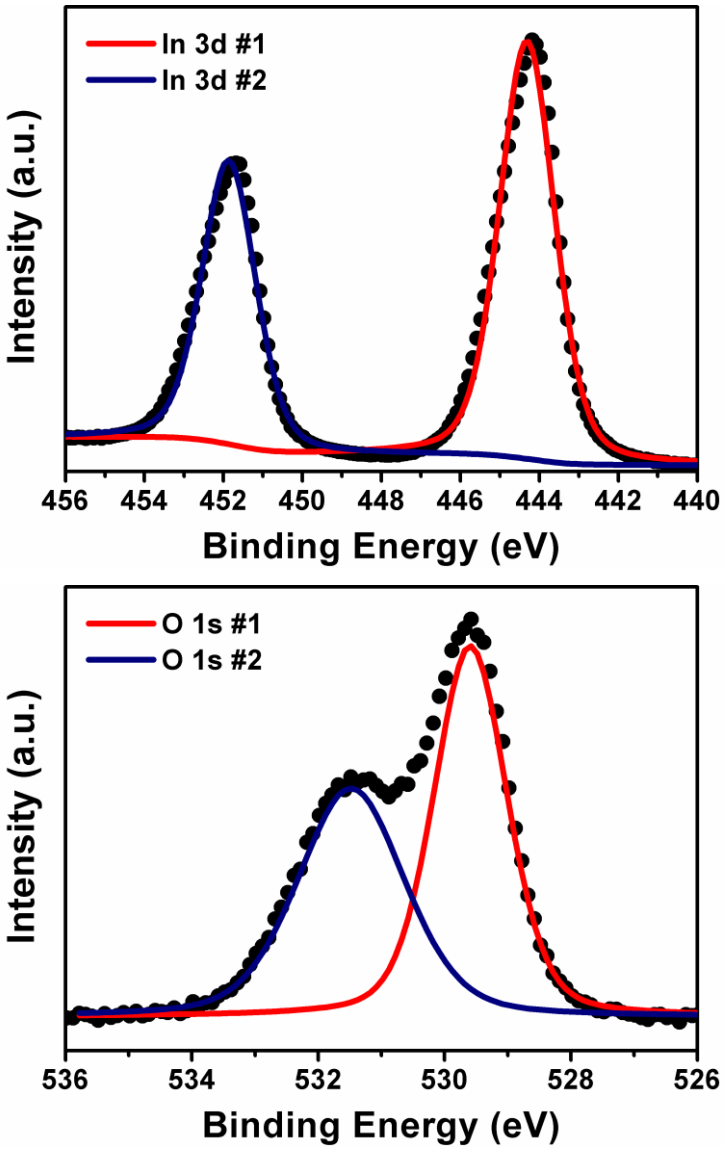

Figure 4.23: In 3d and O 1s XPS high resolution scans of ~10 nm-thick In_2O_3 film deposited at 150 °C.

Figure 4.24 shows the XRD pattern of a 36 nm In_2O_3 film deposited on Si (111) at 150 °C. In the as-deposited state, films were polycrystalline. XRD peaks in Figure 4.24 indicated the cubic In_2O_3 phase, which is known to be highly transparent and conducting.

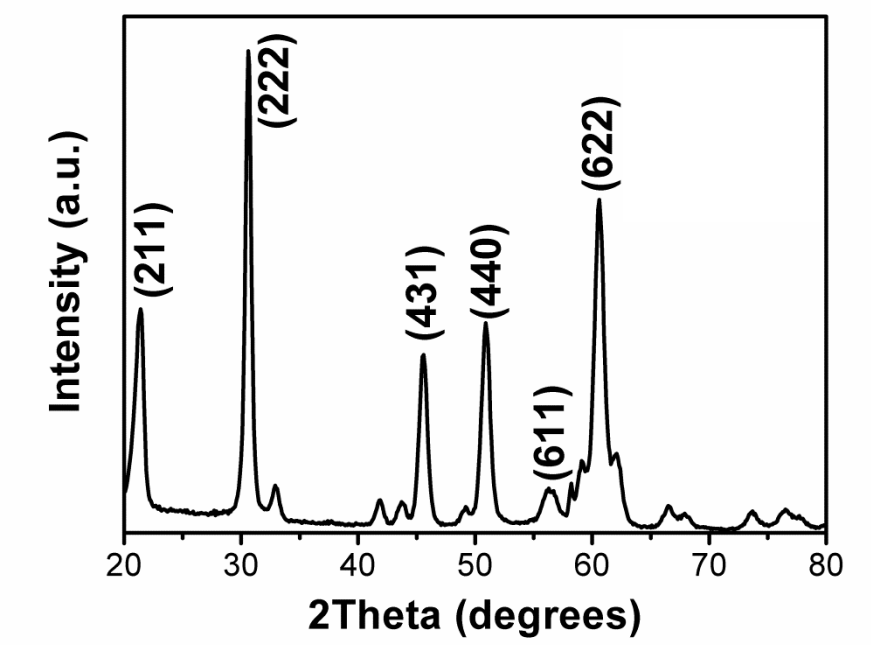

Figure 4.24: XRD pattern of ~36 nm-thick In_2O_3 film representing cubic In_2O_3 phase.

4.3 Characterization of HfO_2 Nanotubes

In order to fabricate HfO_2 nanotubes having different inner diameters, nylon 6,6 nanofibers having different average fiber diameters were obtained by electrospinning technique and these polymeric nanofibers were used as sacrificial templates. In electrospinning, fiber diameters strongly depend on the viscosity of the polymer solution, therefore, the solvent type used and the concentration of the polymer solution are important parameters to control the diameter of the electrospun fibers [81,82]. Uniform and bead-free nylon 6,6 nanofibers having average fiber diameters of ~70 nm and ~330 nm were obtained using different solvent system and polymer concentrations with the viscosities of 0.0228 and 0.115 Pa.s, respectively. Figures. 4.25(a) shows the representative SEM images of electrospun nylon 6,6 nanofibers obtained from 5% (w/v) nylon 6,6 solutions dissolved in HFIP solvent system. Similarly, Figure 4.25(b) is the representative SEM image of nanofibers obtained by the electrospinning of 8% (w/v) nylon 6,6 solution prepared with formic acid

solvent system. Nylon 6,6 nanofibers having much thinner fiber diameters (70±30 nm) were obtained from formic acid solvent system, whereas thicker fibers (330±80 nm) were obtained from HFIP solvent system. This is due to the higher viscosity of the polymer solution in HFIP since less stretching of the electrified jet was occurred for more viscous polymer solutions during the electrospinning process and therefore larger fiber diameters were obtained [81].

In this study, electrospun nylon 6,6 nanofibers having average fiber diameters of ~330 nm and ~70 nm were used as templates for the fabrication of HfO_2 nanotubes (Figs. 4.25(a) and 4.25(b)). Following the deposition of HfO_2 films by thermal ALD on electrospun nanofiber templates, coated samples were calcined in order to obtain HfO_2 nanotubes. The representative SEM images of the nylon 6,6 nanofiber templates after the deposition of 600 cycles HfO_2 at 200°C are presented in Figures 4.25 (c)-(d). As clearly seen from these SEM images, a uniform and conformal HfO_2 layer was deposited on electrospun nanofibers using the self-limiting nature of the ALD process. Desired wall thickness was achieved by adjusting the number of deposited ALD cycles. Figures 4.25 (e)-(f) show the resulting HfO_2 nanotubes obtained by the calcination of HfO_2-coated nylon 6,6 nanofiber templates. For both templates, integrity of the structure was well preserved after the calcination step and a freestanding HfO_2 nanotube network with a uniform and smooth structure was obtained. Flexibility of the samples, however, was lost after the calcination treatment due to the missing polymeric core nanofibers. Samples became brittle and vulnerable to mechanical impacts which may arise during handling. As a result, calcined samples appeared as broken nanotubes in their representative SEM images. Magnified SEM images of HfO_2 nanotubes prepared with electrospun nylon 6,6 nanofiber templates having average fiber diameters of 330 and 70 nm are given in the insets of Figures 4.25(e) and 4.25(f), respectively. Surfaces of the synthesized nanostructures were found to be extremely smooth. Small particle-like structures on the surfaces of individual HNs are due to the ~5 nm Au/Pd alloy deposited on samples prior to SEM imaging.

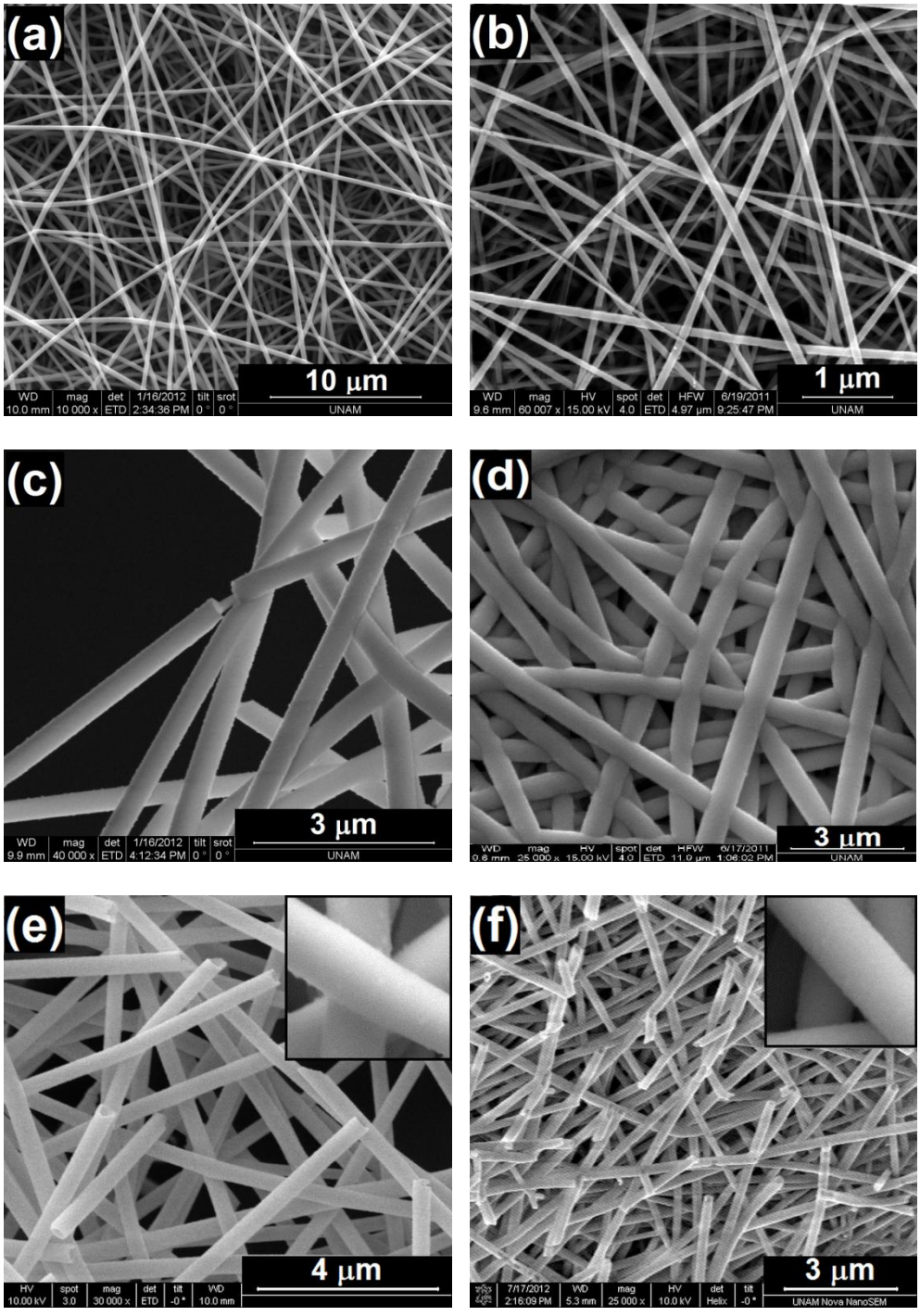

Figure 4.25: Representative SEM images of (a)-(b) electrospun nylon 6,6 nanofibers having ~330 and ~70 nm fiber diameter, (c)-(d) same electrospun nanofibers coated with 600 cycles HfO_2 at 200°C, and (e)-(f) HfO_2 nanotubes obtained by calcination. Insets are the magnified SEM images revealing the surface morphologies of calcined samples.

Both HfO_2 nanotubes with ~70 nm and ~330 nm inner diameters have been characterized in detail and it was observed that they have exhibited very similar chemical and structural properties, so the following data are given only for the HfO_2 nanotube sample having ~330 nm inner diameter. Chemical composition and bonding states of the synthesized HfO_2 nanotubes were studied by XPS. Survey scan detected 25.6 at.% Hf, 58.4 at.% O, and 16.0 at.% C for the HfO_2 nanotubes sample prepared by a nanofiber template having 330 nm average fiber diameter.

Figures 4.26(a)-4.26(b) are the Hf 4f and O 1s high resolution XPS scans, which were fitted by subpeaks in order to reveal the bonding states exist in the material. Hf $4f_{7/2}$ and Hf $4f_{5/2}$ subpeaks of the Hf 4f doublet located at 16.3 and 17.9 eV, respectively, were found to be related to the Hf-O bonding in HfO_2 [83]. O 1s scan (Fig. 4.26(b)) was fitted by two subpeaks located at 529.6 and 531.2 eV, revealing the O-Hf and O-H bonds, respectively [84]. The oxygen concentration corresponding to the O-Hf bond was 49.8 at.% as calculated from the relative integrated intensities of O-Hf and O-H subpeaks. The O-Hf/O-H subpeak ratio (i.e. the ratio of integrated intensities) was found as 5.88, indicating that 85.5% of the O detected in this sample is associated with the formation of HfO_2, corresponding to 49.9 at.% O in the sample. By using this information, Hf:O ratio was calculated as 0.51, and it was concluded that the deposited HfO_2 is almost stoichiometric. Carbon with 16 at.% found in the sample was neither bonded to Hf or O, therefore suggesting surface contamination.

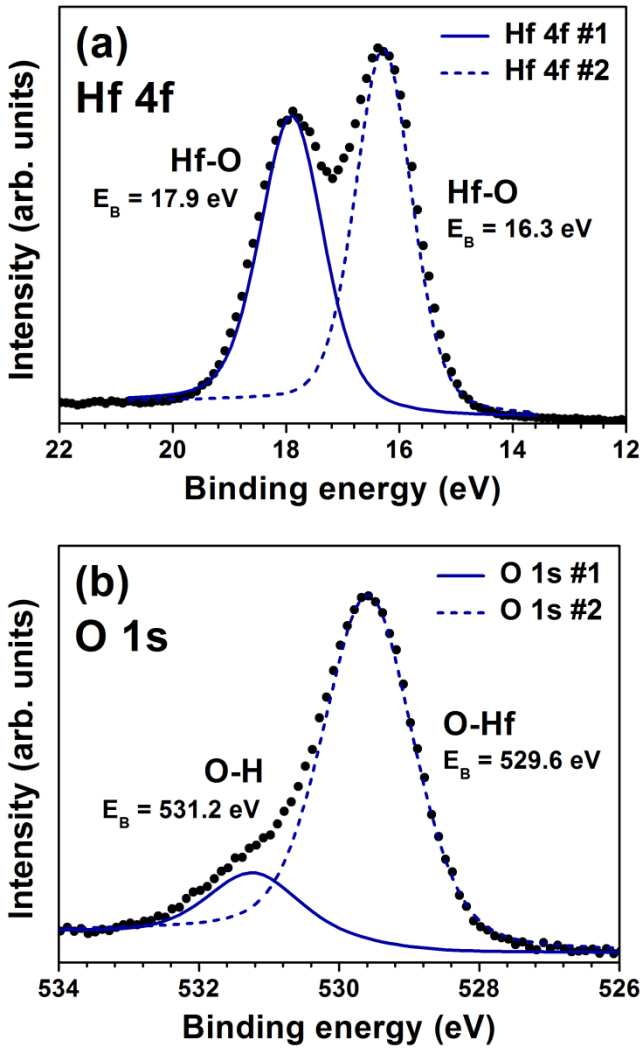

Figure 4.26: (a) Hf 4f doublet and (b) O 1s high resolution XPS scans of the HfO_2 nanotubes with ~330 nm inner diameter.

Figure 4.27 shows the XRD patterns of electrospun nylon 6,6 nanofiber template, template coated with 600 cycles HfO_2, and HfO_2 nanotubes synthesized by the calcination of coated templates at 500°C for 2 hr at air ambient. Electrospun nylon 6,6 nanofiber template has two characteristic peaks at 20.45° and 23.27°. After the deposition of 600 cycles HfO_2, characteristic XRD peaks of the nylon 6,6 nanofiber template disappeared. As-deposited HfO_2 layer was nanocrystalline as determined from the XRD pattern obtained from coated nylon 6,6 nanofibers. Upon calcination at 500°C for 2 hours under air ambient, HfO_2 layer became crystalline with a monoclinic structure, which is the most thermodynamically stable polymorph [85]. This amorphous-to-

polycrystalline transition was in good agreement with the literature reported for HfO_2 thin films annealed at 500°C [86].

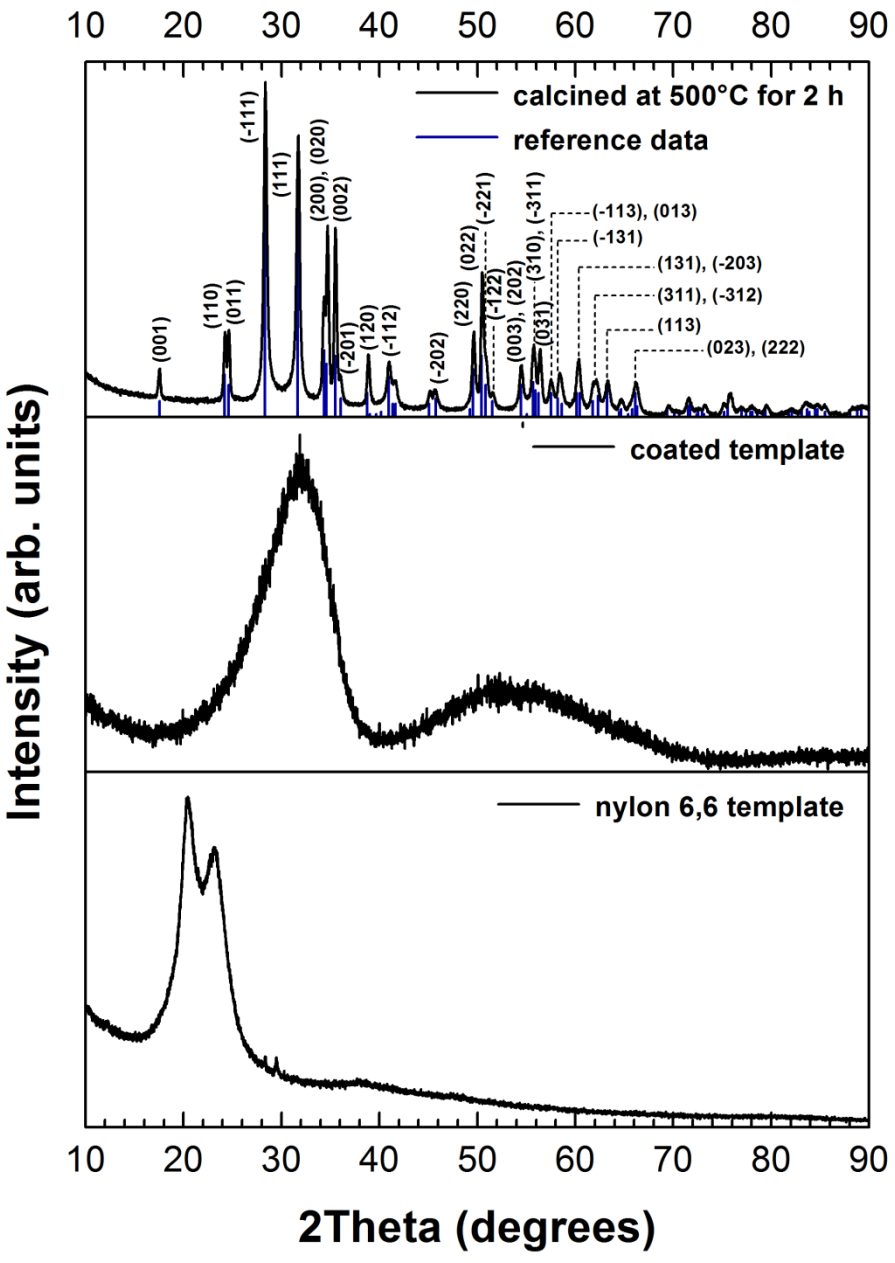

Figure 4.27: . XRD patterns of electrospun nylon 6,6 nanofibers with ~330 nm fiber diameter, nanofiber templates coated with 600 cycles HfO_2 at 200°C using ALD, and the resulting HfO_2 nanotubes after the calcination of coated templates at 500°C under ambient conditions. Reference data for the monoclinic HfO_2 phase is also included (ICDD reference code: 00-034-0104).

Detailed morphology of the HfO_2 nanotubes was studied by TEM, which confirmed the uniform and conformal structure of synthesized HfO_2 nanotubes. Figure 4.28(a) shows the TEM image of HfO_2 nanotubes fabricated by depositing 600 cycles HfO_2 on electrospun nanofibers having average fiber diameter of ~330 nm, followed by a heat treatment carried out under air ambient at 500°C for 2h. Wall thickness was measured as ~65 nm from this image which is quite consistent with the 1.1 Å/cycle deposition rate of HfO_2 ALD at 200°C. When the very identical ALD growth parameters were applied to electrospun nylon 6,6 nanofiber templates having 70±30 nm average fiber diameter, the deposition resulted in a ~15 nm wall thickness (Fig. 4.28(b)). This might be due to the limited exposure time of the partial pressure above the template to reach full saturation, or limited time for diffusion. This claim was tested by performing the same HfO_2 deposition (600 cycles at 200°C, using the same exposure and pulse times) using *exposure mode* on a template having ~70 nm average fiber diameter. In this deposition mode, dynamic vacuum is switched to static vacuum just before the precursor and oxidant pulses, and switched back to dynamic vacuum before the purging periods after waiting for some time and allowing precursor and oxidant molecules to diffuse into the electrospun nanofiber template. This *exposure mode* deposition process resulted in ~65 nm wall thickness as shown in Figure 4.28(c), which supported our postulation. This result indicated that *exposure mode* deposition should be preferred when ALD growth is carried out on high-surface area substrates.

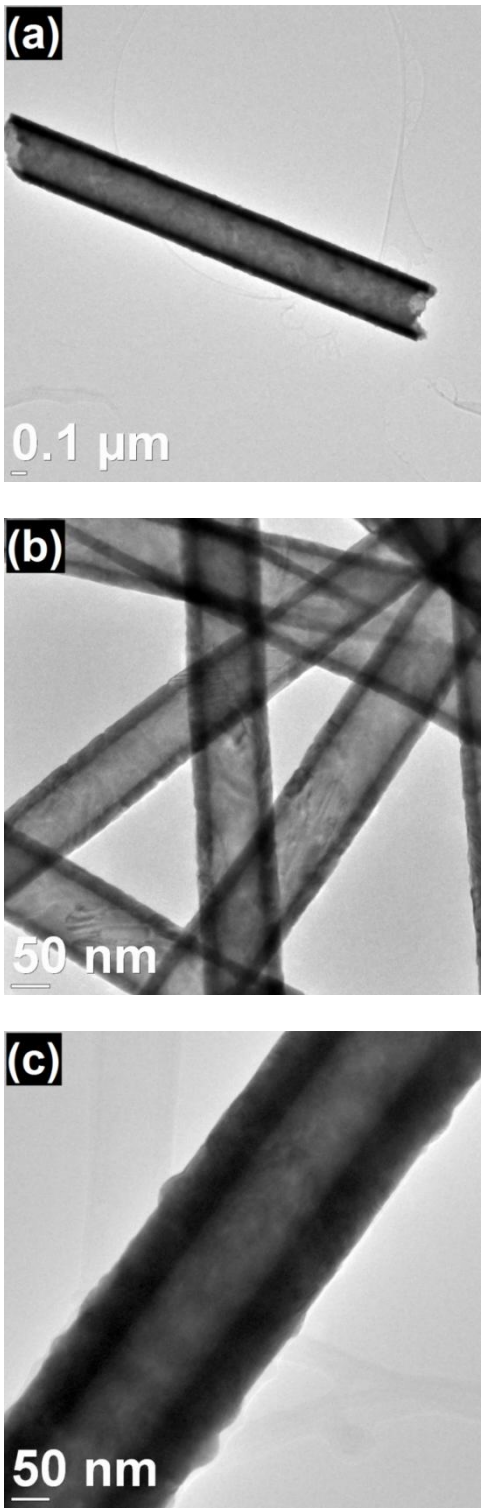

Figure 4.28: TEM images of (a) an individual HfO_2 nanotube deposited by normal mode ALD with an inner diameter of 300 nm and a wall thickness of 65 nm, (b) HfO_2 nanotubes with an inner fiber diameter of 70 nm and a wall thickness of 15 nm deposited by normal mode ALD, (c) HfO_2 nanotubes with an inner fiber diameter of 70 nm and a wall thickness of 65 nm deposited by *exposure mode* ALD.

Figure 4.29 reveals high resolution TEM (HR-TEM) image and the SAED pattern of HfO_2 nanotubes fabricated by depositing 600 cycles HfO_2 on electrospun nanofibers having average fiber diameter of ~330 nm, followed by calcination under air ambient at 500°C for 2h. HR-TEM image of the same sample (Figure 4.29(a)) indicated a polycrystalline structure, which is in good agreement with our XRD results. SAED pattern of the HfO_2 nanotubes (Figure 4.29(b)) consisted of a series of diffraction rings, further revealing the polycrystalline nature of the nanotube sample. Bright spots seen on these polycrystalline diffraction rings are indicators of large crystallite size.

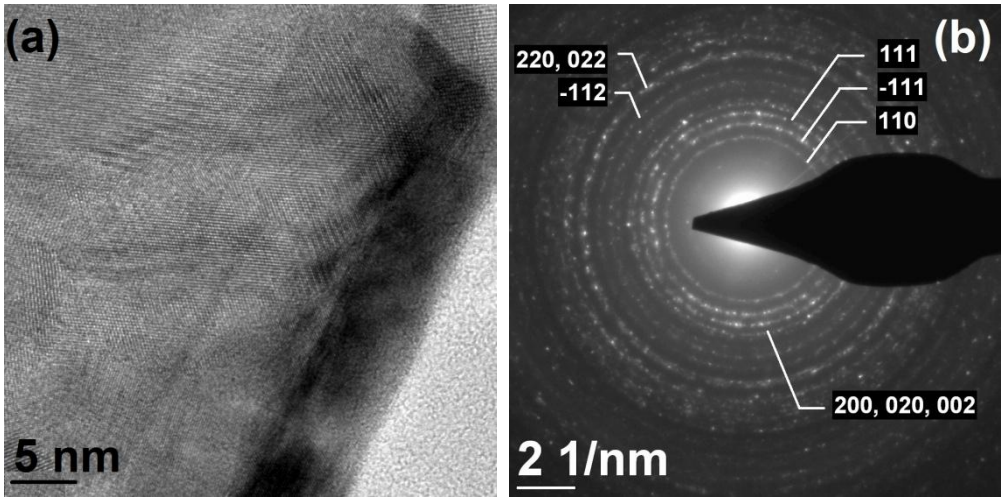

Figure 4.29: (a) HR-TEM image of an individual HfO_2 nanotube with ~330 nm average fiber diameter and ~65 nm wall thickness (b) SAED pattern of the synthesized HfO_2 nanotubes. Most intense peaks are labeled. (ICDD reference code: 00-034-0104)

Chapter 5

Conclusions and Future Directions

Ga_2O_3 thin films were deposited by PEALD using TMG and O_2 plasma, as the gallium precursor and oxidant, respectively. This combination of precursors was not reported in the literature prior to this work. Recipe development steps were presented including the effects of precursor and oxidant doses, purging time and deposition temperature. A significantly wide ALD window from 100 to 400 °C was obtained with a deposition rate of 0.53 Å/cycle. Deposited Ga_2O_3 thin films were characterized in terms of their morphological, elemental, structural, optical and electrical properties. As-deposited films grown within the ALD window were nanocrsytalline. When annealed for 30 minutes under nitrogen (N_2) atmosphere, films became polycrystalline with a monoclinic β-Ga_2O_3 phase for the annealing temperatures starting from 600 °C. As-deposited films were found to be extremely smooth. An increase of the rms roughness value after annealing was caused by the grain formation upon crystallization. Ga_2O_3 films were almost stoichiometric in both as-deposited and annealed states. Optical band gaps of the as-deposited and annealed films were 5.10 and 5.14 eV respectively. Refractive indices of the films increased slightly with post-growth annealing. In order to study capacitance-voltage and current-voltage characteristics of the films, metal-oxide-semiconductor capacitor structures were fabricated using Ga_2O_3 as the

insulating oxide layer. Ga_2O_3 films exhibited decent dielectric properties. Changes in the electrical characteristics with respect to Ga_2O_3 film thickness and annealing temperature were discusssed. Dielectric constant increased with increasing Ga_2O_3 film thickness. Additionally, with an increasing annealing temperature, a slight decrease in dielectric constant was observed, which was attributed to the formation of SiO_2 at the Si-Ga_2O_3 interface.

Effectiveness of the ALD method for coating nanostructured samples with high surface areas was also demonstrated within the scope of this thesis. Hafnia (HfO_2) nanotubes were obtained by following a three-step process: (i) electrospinning of nylon 6,6 nanofibers having different average fiber diameters, (ii) coating of electrospun nylon 6,6 nanofibers by ALD using TDMAH and H_2O as the precursors, and (iii) calcining of coated nanofibers to get rid of the organic content and obtain hollow nanostructures. Different deposition modes were used and compared in detail in terms of their characteristics. As-deposited HfO_2 films were amorphous, however, after calcining at 500 °C for 2 h, polycrystalline nanotubes with a monoclinic structure were obtained.

As a possible follow-up of this study, O_2 plasma saturation might be evidenced and self-limiting growth of In_2O_3 might be optimized. Then, deposition of ternary alloys using In_2O_3 and Ga_2O_3 could be studied. Effect of composition and growth parameters on the deposited films should be studied in detail. Deposition of indium-gallium-oxide (IGO) thin films, which is a novel transparent conducting oxide (TCO), can be optimized. Furthermore, quaternary metal-oxide compounds by adding Zn into IGO (IGZO) can be synthesized which is another promising TCO material. Such ternary and quaternary TCO alloys might be used as channel layers in thin-film-transistors (TFTs) for transparent and flexible electronics applications.

For the template-based nanostructure fabrication via ALD, a wide variety of materials can be synthesized using the similar fabrication route resulting in

functional nanostructures with extremely high surface area which might be attractive for ultra-high sensitivity chemical sensing applications

Bibliography

[1] A.M. Shevjakov, G.N. Kuznetsova, and V.B. Aleskovskii, *Chemistry of High-Temperature Materials*, Proceedings of the Second USSR Conference on High-Temperature Chemistry of Oxides, Leningrad, 1995.

[2] T. Suntola , J. Antson, US Patent 4.058, 430, 1977.

[3] R.L. Puurunen, "Surface chemistry of atomic layer deposition: A case study for the trimethylaluminum/water process," *Journal of Applied Physics*, vol. **97**, pp. 121301-121351, 2005.

[4] M. de Keijser and C. van Opdorp, "Atomic layer epitaxy of gallium arsenide with the use of atomic hydrogen," *Applied Physics Letters*, vol. 58, no. 11, pp. 1187-1189, 1991.

[5] M.T. Bohr et al., *IEEE Spectrum*, pp. 30-35, 2007.

[6] M. Leskela and M. Ritala, "Atomic layer deposition (ALD): from precursors to thin film structures," *Thin Solid Films*, vol. 409, pp. 138–146, 2002.

[7] R.L. Puurunen, "Growth per cycle in atomic layer deposition: A Theorethical Model," *Chemical Vapor Deposition*, vol. 9, no. 5, pp. 249-257, 2003.

[8] J. Becker, "Atomic Layer Deposition of Metal Oxide and Nitride Thin Films," Ph.D. dissertation, Department of Chemistry and Chemical Biology, Cambridge, Massachusetts.

[9] M. Ritala and M. Leskela, " Handbook of Thin Film Materials," *Academic Press*, pp.113, 2002.

[10] S. Heil, "Plasma-Assisted Atomic Layer Deposition of Metal Oxides and Nitrides," Ph.D. dissertation, Technische Universiteit Eindhoven, 2007.

[11] H.B. Profijt et al., "Plasma-Assisted Atomic Layer Deposition: Basics, Opportunities, and Challenges," *Journal of Vacuum Science and Technology A*, vol. 29, pp. 050801-050826, 2011.

[12] G.X. Liu et al., "Electrical properties of Ga_2O_3-based dielectric thin films prepared by plasma enhanced atomic layer deposition (PEALD)," *Journal of Electroceramics*, vol.17, pp.145-149, 2006.

[13] M. Orita et al., "Deep-ultraviolet transparent conductive β-Ga_2O_3 thin films," *Applied Physics Letters,* vol. 77, no. 25, 4166-4168, 2000.
[14] F.K. Shan et al., "Structural, electrical, and optical properties of transparent gallium oxide thin films grown by plasma-enhanced atomic layer deposition," *Journal of Applied Physics,* vol. 98, no. 023504, 2005.

[15] M. Ogita et al., "Presumption and improvement for gallium oxide thin film of high temperature oxygen sensors ," *Applied Surface Science,* vol. 212–213, pp. 397-401, 2003.

[16] S. Fujita, *Proceedings of SPIE* vol.7041, 70410M, 2008.

[17] M. Higashiwaki et al., "Gallium oxide (Ga_2O_3) metal-semiconductor field-effect transistors on single-crystal β-Ga_2O_3 (010) substrates," *Applied Physics Letters,* vol. 100, no. 013504, 2012.

[18] H. Hayashi et al., "Room temperature ferromagnetism in Mn-doped γ-Ga_2O_3 with spinel structure," *Applied Physics Letters,* vol. 89, no. 181903, 2006.

[19] J.H. Kim and P. H. Holloway, "Microstructural characterization of radio frequency magnetron sputter-deposited Ga_2O_3:Mn phosphor thin films," *Journal of Vacuum Science and Technology A,* vol. 20, pp. 928-933, 2002.

[20] N.C. Oldham et al., "Deposition of Ga_2O_3−x ultrathin films on GaAs by e-beam evaporation," *Journal of Vacuum Science and Technology A,* vol. 20, pp. 809-813, 2002.

[21] S.-L. Ou et al., "Growth and etching characteristics of gallium oxide thin films by pulsed laser deposition," *Materials Chemistry and Physics,* vol.133, pp.700-705, 2012.

[22] M. Holland et al., "Ga_2O_3 grown on GaAs by molecular beam epitaxy for metal oxide semiconductor field effect transistors," *Journal of Vacuum Science and Technology B,* vol. 25, pp. 1706-1709, 2007.

[23] H.W. Kim and N. H. Kim, "Growth of gallium oxide thin films on silicon by the metal organic chemical vapor deposition method," *Materials Science and Engineering B,* vol. 110, pp. 34-37, 2004.

[24] L. Kong et al., "Structural and optical properties of heteroepitaxial beta Ga_2O_3 films grown on MgO (100) substrates," *Thin Solid Films,* vol. 520, pp. 4270-4274, 2012.

[25] Y. Kokubun et al., "Sol-gel prepared β-Ga_2O_3 thin films for ultraviolet photodetectors," *Applied Physics Letters,* vol. 90, no. 031912, 2007.

[26] F.K. Shan et al., "Ga_2O_3 thin film deposited by atomic layer deposition with high plasma power," *Integrated Ferroelectrics*, vol. 80, pp. 197-206, 2006.

[27] G.X. Liu et al., "Growth temperature dependence of Ga_2O_3 thin films deposited by plasma enhanced atomic layer deposition," *Integrated Ferroelectrics*, vol. 94, pp. 11-20, 2007.

[28] N.-J. Seong et al., "Electrical characteristics of Ga_2O_3–TiO_2 nanomixed films grown by plasma-enhanced atomic-layer deposition for gate dielectric applications," *Applied Physics Letters*, vol. 87, no. 082909, 2005.

[29] G.X. Liu et al., "Nanomixed TiO_2-Ga_2O_3 thin films grown by plasma enhanced atomic layer deposition (PEALD) method," *Integrated Ferroelectrics*, vol.85, pp. 155-164, 2006.

[30] S.-A. Lee et al., "Metal/Insulator/Semiconductor Structure Using Ga_2O_3 Layer by Plasma Enhanced Atomic Layer Deposition," *Journal of the Korean Physical Society*, vol. 47, pp. S292-S295, 2005.

[31] C. L. Dezelah IV et al., "Atomic Layer Deposition of Ga_2O_3 Films from a Dialkylamido-Based Precursor," *Chemistry of Materials*, vol. 18, pp. 471-475, 2006.

[32] H. Lee et al., "ALD and MOCVD of Ga_2O_3 Thin Films Using the New Ga Precursor Dimethylgallium Isopropoxide, $Me_2GaOiPr$**," *Chemical Vapor Deposition*, vol. 17, pp. 191-197, 2011.

[33] M. Predanocy, "Study of optical and electrical properties of sputtered indium oxide films," *8th International Conference on Advanced Semiconductor Devices & Microsystems (ASDAM)*, pp. 297–300, 2010.

[34] R.B.H Tahar, "Tin doped indium oxide thin films: Electrical properties," *Journal of Applied Physics*, vol. 83, no.5, pp. 2631-2645, 1998.

[35] T. Asikainen, M. Ritala, and M. Leskela, "Atomic layer deposition growth of zirconium doped In2O3 films," *Thin Solid Films*, vol. 440, pp. 152–154, 2003.

[36] C. Brahim et al., "ZrO_2–In_2O_3 thin layers with gradual ionic to electronic composition synthesized by atomic layer deposition for SOFC applications," *Journal of Materials Chemistry*, vol. 19, pp. 760-766, 2009.

[37] M. Ritala, T. Asikainen, and M. Leskela, "Enhanced Growth Rate in Atomic Layer Epitaxy of Indium Oxide and Indium-Tin Oxide Thin Films," *Electrochemical and Solid-State Letters*, vol. 1, no. 3, pp. 156-157, 1998.

[38] D.-J. Lee et al., "Self-Limiting Film Growth of Transparent Conducting In_2O_3 by Atomic Layer Deposition using Trimethylindium and Water Vapor" *The Journal of Physical Chemistry C*, vol. 115, no. pp. 15384-15389, 2011

[39] O. Nilsen et al., "Thin films of In_2O_3 by atomic layer deposition using $In(acac)_3$," *Thin Solid Films*, vol. 517, pp. 6320–6322, 2009..

[40] A. Dameron et al., "Conductive Conformal Thin Film Coatings for Textured PV, ALD versus Sputtering," *Proceedings of SPIE*, vol. 8110, pp. 81100M-81100M6, 2011.

[41] J.W. Elam et al., "Atomic Layer Deposition of In_2O_3 Using Cyclopentadienyl Indium: A New Synthetic Route to Transparent Conducting Oxide Films," *Chemistry of Materials*, vol. 18, pp. 3571-3578, 2006.

[42] J.A. Libera, J.N. Hryn, and J.W. Elam, "Indium Oxide Atomic Layer Deposition Facilitated by the Synergy between Oxygen and Water," *Chemistry of Materials*, vol. 23, pp. 2150-2158, 2011.

[43] Y.-S. Min et al., "Atomic Layer Deposition of $Bi_{1-x-y}Ti_xSi_yO_z$ Thin Films from Alkoxide Precursors and Water," *Journal of The Electrochemical Society*, vol. 152, no. 9, pp. F124-F128, 2005.

[44] A.B.F. Martinson et al., "ZnO Nanotube Based Dye-Sensitized Solar Cells," *Nano Letters*, vol. 7, no. 8, pp. 2183-2187, 2007.

[45] Y.-H. Chang et al., "Fabrication and Characteristics of Self-Aligned ZnO Nanotube and Nanorod Arrays on Si Substrates by Atomic Layer Deposition," *Journal of The Electrochemical Society*, vol. 157, no. 11, pp. K236-K241, 2010.

[46] J. Lee et al., "Atomic layer deposition of TiO_2 nanotubes and its improved electrostatic capacitance," *Electrochemistry Communications*, vol. 12, pp. 210-212, 2010.

[47] Y. Qin et al., "Atomic Layer Deposition Assisted Template Approach for Electrochemical Synthesis of Au Crescent-Shaped Half-Nanotubes," *ACS Nano*, vol. 5, no. 2, pp. 788-794, 2011.

[48] J. Hwang et al., "Al_2O_3 Nanotubes Fabricated by Wet Etching of ZnO/Al_2O_3 Core/Shell Nanofibers," *Advanced Materials*, vol. 16, no.5, pp. 422-425, 2004.

[49] J.S. Lee et al., "Al_2O_3 nanotubes and nanorods fabricated by coating and filling of carbon nanotubes with atomic-layer deposition," *Journal of Crystal Growth*, vol. 254, pp. 443-448, 2003.

[50] Q. Peng et al., "Bi-directional Kirkendall Effect in Coaxial Microtube Nanolaminate Assemblies Fabricated by Atomic Layer Deposition," *ACS Nano*, vol. 3, no. 3, pp. 546-554, 2009.

[51] P. Heikkilä et al., "High surface area nanostructured tubes prepared by dissolution of ALD-coated electrospun fibers," *Journal of Materials Science*, vol. 47, pp. 3607-3612, 2012.

[52] B.-S. Lee et al., "Fabrication of SnO_2 nanotube microyarn and its gas sensing behavior," *Smart Materials and Structures*, vol. 20, no. 105019, 2011.

[53] G.-M. Kim et al., "Nanostructured Pure Anatase Titania Tubes Replicated from Electrospun Polymer Fiber Templates by Atomic Layer Deposition," *Chemistry of Materials*, vol. 20, no. 9, pp. 3085-3091, 2008.

[54] E. Santala et al., "The preparation of reusable magnetic and photocatalytic composite nanofibers by electrospinning and atomic layer deposition," *Nanotechnology*, vol. 20, pp. 035602-035606, 2009.

[55] S.-W. Choi et al., "Synthesis of Highly Crystalline Hollow TiO_2 Fibers Using Atomic Layer Deposition on Polymer Templates," *Journal of The American Ceramic Society*, vol. 94, no. 7, pp. 1974-1977, 2011.

[56] J.Y. Park et al., "Synthesis and Gas Sensing Properties of TiO_2–ZnO Core-Shell Nanofibers," *Journal of The American Ceramic Society*, vol. 92, pp. 2551-2554, 2009.

[57] S.-W. Choi, J.Y. Park, and S.S. Kim, "Synthesis of SnO_2–ZnO core–shell nanofibers via a novel two-step process and their gas sensing properties," *Nanotechnology*, vol. 20, pp. 465603-465608, 2009.

[58] J.Y. Park, S.-W. Choi, and S.S. Kim, "A synthesis and sensing application of hollow ZnO nanofibers with uniform wall thicknesses grown using polymer templates," *Nanotechnology*, vol. 21, pp. 475601-475609, 2010.

[59] L.X. Liu et al., "Photoluminescence of rare earth3+ doped uniaxially aligned HfO_2 nanotubes prepared by sputtering with electrospun polyvinylpyrolidone nanofibers as templates," *Journal of Applied Physics*, vol. 107, no. 2, pp. 0243091-0243095, 2010.

[60] X. Qiu et al., "Size control of highly ordered HfO_2 nanotube arrays and a possible growth mechanism," *Nanotechnology*, vol. 20, pp. 455601-455609, 2009.

[61] P. Banerjee, W.-A. Chiou, and G.W. Rubloff, "Crystallization Behavior of HfO_2 Nanotubes in Different Environments ," *Microscopy and Microanalysis*,

vol. 15, no. 2, pp. 1250-1252, 2009.

[62] D. Gu et al., "Atomic Layer Deposition of ZrO_2 and HfO_2 Nanotubes by Template Replication," *Electrochemical and Solid-State Letters*, vol. 12, no. 4, pp. K25-K28, 2009.

[63] I. Perez et al., "TEM-Based Metrology for HfO_2 Layers and Nanotubes Formed in Anodic Aluminum Oxide Nanopore Structures," *Small*, vol. 4, no. 8, pp. 1223-1232, 2008.

[64] T.M. Abdel-Fattah, D. Gu and H. Baumgart, "Nanocomposites of ALD Hafnia Nanotubes Surface Functionalized with Gold Nanoparticles," *ECS Transactions*, vol. 41, no. 2, pp. 139-144, 2011.

[65] M. Shandalov and P.C. McIntyre, "Size-dependent polymorphism in HfO_2 nanotubes and nanoscale thin films," *Journal of Applied Physics*, vol. 106, no. 8, pp. 084322, 2009.

[66] Y.Il Song, C.-M. Yang, and L.K. Kwac, "Atomic layer coating of hafnium oxide on carbon nanotubes for high performance field emitters," *Applied Physics Letters*, vol. 99, no. 15, pp. 153115, 2011.

[67] G. Binnig, C. F. Quate, and C. H. Gerber, "Atomic Force Microscope," *Physical Review Letters*, vol. 56, no. 9, pp. 930-934, 1996.

[68] From the website: http://www.panalytical.com/index.cfm?pid=314

[69] Y.T. Moon, US Patent US Patent 8039362, 2011.

[70] F. Shi, Y. Liu, and Q. Sun, "Analysis to microstructure of CuO/SiO_2 composite thin films annealing at different atmosphere," *Pan Tao Ti Hsueh Pao/ Chinese Journal of Semiconductors*, vol. 29, no. 12, pp. 2381-2384, 2008.

[71] J. Moser and F. Levy, "Growth mechanisms and near-interface structure in relation to orientation of MoS_2 sputtered thin films," *Journal of Materials Research*, vol. 7, no. 3, pp. 734-740, 1992.

[72] D. K. Pawar et al., "Synthesis of nanocrystalline nickel-zinc ferrite ($Ni_{0.8}Zn_{0.2}Fe_2O_4$) thin films by chemical bath deposition method," *Journal of Alloys and Compounds*, vol. 509, no. 8, pp. 3587-3591, 2011.

[73] D. H. Kim et al., "Chemical Vapor Deposition of Ga_2O_3 Thin Films on Si Substrates," *Bulletin of the Korean Chemical Society*, vol. 23, no. 2, pp. 225-228, 2002.

[74] V. K. Josepovits et al., “Effect of gas adsorption on the surface structure of β-Ga_2O_3 studied by XPS and conductivity measurements,” *Sensors and Actuators B*, vol. 48, pp. 373-375, 1998.

[75] M. Rebien et al., “Optical properties of gallium oxide thin films,” *Applied Physics Letters*, vol. 81, no. 2, pp. 250-252, 2002.

[76] From the website:
http://www.doitpoms.ac.uk/tlplib/ellingham_diagrams/interactive.html

[77] H. Zhang and R. Solanki, “Atomic layer deposition of high dielectric constant nanolaminates,” *Journal of the Electrochemical Society*, vol. 148, no. 4, pp. F63-F66, 2001.

[78] K. Natori, D. Otani, and N. Sano, “Thickness dependence of the effective dielectric constant in a thin film capacitor,” *Applied Physics Letters*, vol. 73, no. 5, pp. 632-634, 1998.

[79] J. Oh et al., “The dependence of dielectric properties on the thickness of (Ba,Sr)TiO_3 thin films,” *Current Applied Physics*, vol. 7, pp. 168–171, 2007.

[80] A. Goswami, “Thin Film Fundamentals,” New Age International Publishers, pp. 390, 2005.

[81] S. Ramakrishna et al., “An Introduction to Electrospinning and Nanofibres,” *World Scientific Publishing Co. Ltd*., Singapore, 2005.

[82] T. Uyar and F. Besenbacher, “Electrospinning of uniform polystyrene fibers: The effect of solvent conductivity,” *Polymer*, vol. 49, pp. 5336-5343, 2008.

[83] M.-H. Cho et al., “Thermal stability and structural characteristics of HfO_2 films on Si (100) grown by atomic-layer deposition,” *Applied Physics Letters*, vol. 81, no.3, pp. 472-474, 2002.

[84] D.-P. Kim et al., “Dry Etching of High-k Dielectric Thin Films in HBr/Ar Plasma,” *Journal of the Korean Physical Society*, vol. 54, no. 2, pp. 934-938, 2009.

[85] G. Štefanić, S. Musić, and K. Molčanov, “The crystallization process of HfO_2 and ZrO_2 under hydrothermal conditions,” *Journal of Alloys and Compounds*, vol. 387, pp. 300–307, 2005.

[86] Y.-K. Chiou, C.-H. Chang, and T.-B. Wu, “Characteristics of hafnium oxide grown on silicon by atomic-layer deposition using tetrakis

(ethylmethylamino) hafnium and water vapor as precursors," *Journal of Materials Research*, vol. 22, no. 7, pp. 1899-1906, 2007.